Journal Pre-proofs

Research article

Unravelling the ion transport and the interphase properties of a mixed olivine cathode for Na-ion battery

Luca Minnetti, Leonardo Sbrascini, Antunes Staffolani, Vittorio Marangon, Francesco Nobili, Jusef Hassoun

PII: S2095-4956(24)00313-9
DOI: https://doi.org/10.1016/j.jechem.2024.04.028
Reference: JECHEM 3832

To appear in: *Journal of Energy Chemistry*

Received Date: 20 March 2024
Revised Date: 20 April 2024
Accepted Date: 20 April 2024

Please cite this article as: L. Minnetti, L. Sbrascini, A. Staffolani, V. Marangon, F. Nobili, J. Hassoun, Unravelling the ion transport and the interphase properties of a mixed olivine cathode for Na-ion battery, *Journal of Energy Chemistry* (2024), doi: https://doi.org/10.1016/j.jechem.2024.04.028

This is a PDF file of an article that has undergone enhancements after acceptance, such as the addition of a cover page and metadata, and formatting for readability, but it is not yet the definitive version of record. This version will undergo additional copyediting, typesetting and review before it is published in its final form, but we are providing this version to give early visibility of the article. Please note that, during the production process, errors may be discovered which could affect the content, and all legal disclaimers that apply to the journal pertain.

© 2024 Published by ELSEVIER B.V. and Science Press on behalf of Science Press and Dalian Institute of Chemical Physics, Chinese Academy of Sciences

Journal Pre-proofs

Unravelling the ion transport and the interphase properties of a mixed olivine cathode for Na-ion battery

Luca Minnetti[a], Leonardo Sbrascini[a], Antunes Staffolani[a,b], Vittorio Marangon[c,d], Francesco Nobili[a,e,*], Jusef Hassoun[c,d,f,*]

[a] *School of Sciences and Technologies – Chemistry Division, University of Camerino, Via Madonna delle Carceri ChIP, 62032, Camerino, Italy*

[b] *Current affiliation: University of Bologna, Department of Chemistry "Giacomo Ciamician", Via Francesco Selmi 2, 40126, Bologna, Italy*

[c] *Graphene Labs, Istituto Italiano di Tecnologia, via Morego 30, Genoa, 16163, Italy*

[d] *Department of Chemical, Pharmaceutical and Agricultural Sciences, University of Ferrara, Via Fossato di Mortara 17, 44121, Ferrara, Italy*

[e] *GISEL − Centro di Riferimento Nazionale per i Sistemi di Accumulo Elettrochimico di Energia, INSTM, Firenze 50121, Italy*

[f] *National Interuniversity Consortium of Materials Science and Technology (INSTM) University of Ferrara Research Unit, University of Ferrara, Via Fossato di Mortara, 17, 44121, Ferrara, Italy*

[*]Corresponding authors.

E-mail addresses: jusef.hassoun@unife.it (J. Hassoun), francesco.nobili@unicam.it (F. Nobili)

ABSTRACT

The replacement of Li by Na in an analogue battery to the commercial Li-ion one appears a sustainable strategy to overcome the several concerns triggered by the increased demand for the electrochemical energy storage. However, the apparently simple change of the alkali metal represents a challenging step which requires notable and dedicated studies. Therefore, we investigate herein the features of a $NaFe_{0.6}Mn_{0.4}PO_4$ cathode with triphylite structure achieved from the conversion of a $LiFe_{0.6}Mn_{0.4}PO_4$ olivine for application in Na-ion battery. The work initially characterizes the structure, morphology and performances in sodium cell of

Journal Pre-proofs

$NaFe_{0.6}Mn_{0.4}PO_4$, achieving a maximum capacity exceeding 100 mAh g^{-1} at a temperature of 55 °C, and adequate rate capability, and suitable retention confirmed by ex-situ measurements. Subsequently, the study compares in parallel key parameters of the $NaFe_{0.6}Mn_{0.4}PO_4$ and $LiFe_{0.6}Mn_{0.4}PO_4$ such as Na^+/Li^+ ions diffusion, interfacial characteristics, and reaction mechanism in Na/Li cells using various electrochemical techniques. The data reveal that relatively limited modification of $NaFe_{0.6}Mn_{0.4}PO_4$ chemistry, structure and morphology compared to $LiFe_{0.6}Mn_{0.4}PO_4$ greatly impact the reaction mechanism, kinetics and electrochemical features. These changes are ascribed to the different physical and chemical features of the two compounds, the slower mobility of Na^+ with respect to Li^+ , and a more resistive electrode/electrolyte interphase of sodium compared with lithium. Relevantly, the study reveals analogue trends of the charge transfer resistance and the ion diffusion coefficient in $NaFe_{0.6}Mn_{0.4}PO_4$ and $LiFe_{0.6}Mn_{0.4}PO_4$ during the electrochemical process in half-cell. Hence, the $NaFe_{0.6}Mn_{0.4}PO_4$ achieved herein is suggested as a possible candidate for application in a low-cost, efficient, and environmentally friendly Na-ion battery.

Keywords: $NaFe_{0.6}Mn_{0.4}PO_4$; Olivine; Na-ion; Ion transport; Interphase

1. Introduction

Energy production has been worldwide moving toward renewable sources such as solar, wind, and geothermal to overcome the various drawbacks presently attributed to the massive use of fossil fuels [1,2]. The intermittent nature of these sources has triggered efficient, cheap, and environmentally sustainable energy storage systems (ESS) for an actual stabilization of the power grid [3]. Among the several adequate systems, the electrochemical energy storage and, in particular, the rechargeable batteries have played the most relevant role in the last decade due to their versatility both in a relatively small scale, such as the portable electronics, and in a much larger scale including the hybrid and full-electric vehicles (HEVs and EVs) as well as the renewable power production plants [4,5]. The rapid diffusion of EVs and the growing stationary use of renewable energies, recently adopted for hindering excessive greenhouse gases emission, increased the demand for efficient, low cost, and sustainable batteries able to satisfy these diversified markets [6,7]. Certainly, the lithium-ion battery (LIB) has been the most widely diffused energy storage systems since 1990 due to a high energy density, that recently exceeded 280 Wh kg^{-1}, and an outstanding cycle life ascribed to the efficient Li *rocking-chair* mechanism promoted by the intercalation processes at the layered metal oxide cathode and the graphite anode [8]. Furthermore, several challenging requests of the modern EVs market [7,9], including the long driving range and the high safety, have triggered R&D for new LIBs configurations with alternative chemistries at the anode, cathode, and electrolyte in order to improve the cell performances [10]. However, the massive use of lithium and its compounds for fulfilling this increasing demand posed serious economical and geopolitical concerns, mainly ascribed to the raising price and the local availability of this important alkali metal [11]. A possible solution of this challenging problem

Journal Pre-proofs

ascribed to the LIB may be represented by the development of an analogue battery using a different and more abundant alkali metal, such as the sodium-ion battery (SIB) [12,13]. Despite the lower capacity and a higher electrochemical potential than lithium (3860 mAh g^{-1} and -3.04 V vs. SHE for Li and 1860 mAh g^{-1} and -2.71 V vs. SHE for Na), sodium appeared more sustainable due to its abundance and homogeneous distribution on the Earth crust [14,15]. In addition, SIBs based on layered metal oxides cathodes and carbon-based anodes have been indicated to exploit an analogue reaction mechanism to LIB, thereby possibly facilitating the R&D for alternative energy storage systems based on Na [16]. On the other hand, economic and environmental issues of transition metals included in layered oxide composition such as cobalt, and possible delamination with phase transition and deterioration of these electrodes during cell operation have promoted the use of polyanionic phospho-olivines characterized by remarkable stability, low cost and non-toxicity [17]. Among them, lithium iron phosphate ($LiFePO_4$) revealed a specific capacity of 170 mAh g^{-1} [18,19], a potential of 3.45 V vs. Li^+/Li, thus an energy density of ~70% compared to diffused layered oxides such as $LiNi_{0.33}Co_{0.33}Mn_{0.33}O_2$ (210 mAh g^{-1} at 3.8 V vs. Li^+/Li), however a relevantly longer cycle life and a 40% lower price which promoted its wide commercialization over the last decade, in particular for the stationary storage [20,21]. The partial substitution of iron with other transition metals with a higher redox potential, such as Mn or Ni into a "mixed-olivine" with general formula $LiFe_{1-x}M_xPO_4$ appeared an adequate strategy to increase the energy density of the olivine cathodes [22–24]. The multi-metal concept can in fact lead to mixed olivine with a higher potential than $LiFePO_4$ [22], due to redox couples such as Mn^{+2}/Mn^{+3} (3.8 V vs. Li^+/Li), still holding acceptable electronic conductivity, efficient Li^+ transport [25,26], and hindered pseudo Jahn-Teller distortion, which is typically limited by the presence of Fe [27,28]. For these reasons $LiFe_{1-x}M_xPO_4$ cathodes are currently used in commercial Li-ion batteries delivering higher energy density compared to the LFP system [29]. The mixed olivine can electrochemically react with Li according to a two-phase mechanism (similarly to $LiFePO_4$), or include a single-phase charge-transfer process with formation of a solid-solution, depending on the ratio between Fe and the other metals [30,31]. $NaFePO_4$ cathode can in principle perform similarly to $LiFePO_4$ using the abundant and economically sustainable sodium instead of lithium [32,33], however with a lower theoretical specific capacity (154 mAh g^{-1}) and potential (3.1 V vs. Na^+/Na) as well as slower kinetics due to the less electronegative and larger alkali metal [34]. A relevant drawback of the $NaFePO_4$ prepared using conventional synthetic pathways has been represented by the predominant formation of the electrochemically inactive polyanionic phosphates with the maricite structure [35,36], which is characterized by the absence of cationic channels suitable for allowing Na^+ transport [37,38]. Moreover, $NaMnPO_4$ can be characterized by the presence of the electrochemically inactive natrophilite phase, in which Na and Mn exchange their positions leading to antisite mixing where half of the of the Na ions occupies M1 sites and the other half occupies M2 sites [39]. Instead, electrochemically active triphylite-type $NaFePO_4$ has been achieved through conversion strategies involving electrochemical or chemical

de-lithiation of $LiFePO_4$ and subsequent sodiation of heterosite $FePO_4$.[40,41]. The ion-exchange was considered a reasonable method to obtain Na-based olivine cathode, On the other hand, the lithium extracted from the LFMP precursor during the electrochemical formation (de-lithiation) step can be recovered from the electrolyte by simple evaporation, and reused for olivine precursor or electrolytes preparation into a green-loop which actually limits the overall impact of the process [42]. The need for large-scale diffusion of post-lithium materials for energy storage has triggered relevant research for developing $NaFePO_4$ electrodes with increased capacity and energy density [43,44]. In analogy with the $LiFePO_4$, a suitable strategy to improve the performances of the $NaFePO_4$ has been the partial substitution of iron with others transition metals to achieve a mixed-olivine version of the electrode [45]. In particular, the manganese-to-iron substitution to achieve the $NaFe_{1-y}Mn_yPO_4$ triphylite appeared one of the most promising pathways to achieve efficient Na^+ insertion/de-insertion electrochemical process into the olivine structure [46]. Despite the first Mn-doped $NaFePO_4$ was already achieved in 2011 [47], only few detailed studies of sodium-based mixed olivine cathodes have been reported in literature, particularly focusing on the degree of Mn substitution [45] and the associated effect on the structure and on the Na^+ insertion/extraction mechanism [46]. Accordingly, we exploited in this work the electrochemical conversion of a $LiFe_{0.6}Mn_{0.4}PO_4$ olivine cathode previously synthetized to the analogue $NaFe_{0.6}Mn_{0.4}PO_4$ [24]. This mixed olivine can hold good electronic conductivity and efficient Li^+ transport, in spite of the pseudo Jahn-Teller distortion due to the Mn. On the other hand, the Mn content of 0.4 can increase the energy density of the material. The conversion process has been fully monitored by X-ray diffraction, Raman spectroscopy, and Coupled Plasma–Optical Emission Spectroscopy (ICP-OES) and the obtained $NaFe_{0.6}Mn_{0.4}PO_4$ studied in terms of electrochemical features in sodium cell. The sodium-olivine cathode has been investigated by means of cyclic voltammetry, galvanostatic intermittent titration technique, electrochemical impedance spectroscopy at different states of charge with distribution of relaxation time function, and compared with the lithium analogue. These efforts have clarified the analogies and the differences between NFMP and LFMP in terms of alkali ions diffusion coefficient, interphase features, and charge-transfer properties. In addition, the work reported the stability of the NFMP cathode for over 100 cycles, and revealed the effect of the temperature on the characteristics of the related sodium cell which is a key factor for boosting the battery performances. The achieved results can shed light on reaction kinetics, interfacial properties, and ions diffusion in order to improve the features of the mixed-olivine cathodes for application in Na-ion battery.

2. Experimental

2.1. Synthesis of $LiFe_{0.6}Mn_{0.4}PO_4$ and conversion to $NaFe_{0.6}Mn_{0.4}PO_4$ electrode

$LiFe_{0.6}Mn_{0.4}PO_4$ olivine (subsequently indicated with the acronym LFMP) was synthetized by sol–gel precipitation of the precursors and subsequent annealing at 850 °C under argon according to a procedure reported in detail in previous works

[23,24]. Electrodes of this material were prepared by doctor blade casting of LFMP on aluminum foils (thickness of 20 μm). The slurries were prepared by dispersing in a beaker the active material, poly(vinylidene fluoride) (PVDF 6020, Solef Solvay), and Super P carbon (Timcal) with an 8:1:1 weight ratio, respectively, in N-methyl-pyrrolidone (Sigma Aldrich), and stirring at room temperature until homogenization (about 2 h). The electrode foils were dried for about 4 h on a hot plate at 70 °C, cut into the form of disks with diameter of 10 mm, pressed with a hydraulic tool (Perkin-Elmer) for 30 s at 6.37 ton cm^{-2}, and dried for 3 h at 120 °C under vacuum to remove residual traces of water or solvent. The active material loading ranged from 3 to 3.5 mg cm^{-2} as normalized to the electrode geometric area (0.785 cm^2). The $NaFe_{0.6}Mn_{0.4}PO_4$ (indicated with the acronym NFMP) was achieved throughout galvanostatic de-lithiation of LFMP to $Fe_{0.6}Mn_{0.4}PO_4$ (indicated with the acronym FMP) by charging in Li-cell, and subsequent galvanostatic sodiation by discharging in Na-cell (see subsequent paragraphs for cell assembly and tests) [41]. Carbon coated Al electrodes were prepared by the doctor blade casting procedure above described using Super P carbon and PVDF binder in the 80:20 weight ratio, cut into 10 mm disks, and dried 3 h at 120 °C under vacuum.

2.2. Electrodes Characterization

Scanning electron microscopy (SEM) images of the LFMP, FMP, and NFMP electrodes and the energy dispersive X-ray spectroscopy (EDS) spectra were collected using a Zeiss Sigma 300 FE-SEM equipped with Bruker QUANTAX EDX detector. The elemental composition of LFMP, FMP, and NFMP was determined via Inductively Coupled Plasma–Optical Emission Spectroscopy (ICP-OES) technique. HNO_3 (70%, ≥99.999% trace metal basis, Sigma-Aldrich) and HCl (37%, for analysis-ISO, Carlo Erba reagents) were used without any further purifications. Ultrapure H_2O (18 MΩ cm) was used for the dilution of the samples. The powder recovered from the electrodes (about 4 mg of active material) was digested in 1 mL of aqua regia (HNO_3:HCl 1:3 molar ratio) at 120 °C for 1 h by using a Parr 4744 acid digestion vessel (Parr Instrument Company). After cooldown, the solutions were diluted to the proper concentration prior the ICP-OES analysis. An ICP-OES iCAP Pro 11160 (ThermoFischer Scientific) was used for the element determination. X-ray diffraction (XRD) patterns of the LFMP, FMP, and NFMP electrodes leaned on a glass sample holder were collected through a Bruker D8 Advance instrument using a Cu Kα source and a graphite monochromator of the different beam by performing scans in the 2θ range from 15° to 60° at a rate of 10 s $step^{-1}$ with a step size of 0.02°. Rietveld refinement of LFMP, FMP, and NFMP patterns was carried out through the MAUD software [48] by using the reference parameters of $LiFe_{0.78}Mn_{0.22}PO_4$ (*Pnma* space group, N. 62, ICSD #193641) [49], $Mn_{0.8}Fe_{0.2}PO_4$ (*Pnma* space group, N. 62, ICSD #166750) [50], and $NaMn_{0.93}Fe_{0.07}PO_4$ (*Pnma* space group, N. 62, ICSD #26006) [51] samples for LFMP, FMP, and NFMP, respectively. The atomic displacement parameters have been forced to have the same value for Fe, Mn, alkali metal (Li or Na), and the PO_3^- anions. The weighted-profile (R_{wp}%) and goodness-of-fit (*GOF*) values were <15 and <1.5, respectively. Raman Spectroscopy

was performed on the LFMP, FMP, and NFMP electrodes through a Czerny-Turner spectrometer (iHR320 Horiba Scientific) equipped with a diffraction grating of 1800 grooves mm^{-1} and a laser source with λ = 532 nm. Before the analysis FMP and NFMP electrodes, recovered after de-lithiation and sodiation processes, respectively, were washed with DMC solvent and dried under vacuum for 30 minutes.

2.3. Cells assembly

Swagelok-type polypropylene cell with either two-electrode or three-electrode configuration, and CR-2032 coin-type cells (MTI Corp.) were used in this work. The Swagelok-type cells were assembled by staking 10 mm-diameter working electrode, 10 mm-diameter glass fiber (Whatman® GF/A*)* as the separator soaked with the electrolyte, and 10 mm-diameter disk of either Li or Na as counter electrode. An additional 10 mm-diameter disk of the respective alkali metal was used as the reference electrode to modify the two-electrode to the three-electrode setup. Additional three-electrode Swagelok-type sodium cells were prepared using a 10 mm-diameter Super P Carbon/PVDF electrode (SP-Al) as cathode, a 10 mm-diameter sodium metal anode, a 10 mm-diameter Whatman® GF/B as the separator, and another 10 mm sodium metal disk as the reference electrode. The coin-type cells were assembled by stacking 10 mm-diameter working electrode, 16 mm-diameter glass fiber (Whatman® GF/A) as the separator, and 14 mm-diameter counter electrode of either Li or Na. The electrolyte for the Li-cells was a solution of $LiPF_6$ (1 M) in ethylene carbonate/dimethyl carbonate (EC:DMC 1:1 by volume, battery grade, Sigma Aldrich), and for Na-cells a 1 M solution of $NaPF_6$ in ethylene carbonate/propylene carbonate (EC:PC 1:1 by volume, battery grade, Sigma Aldrich) with 2% in weight of fluoroethylene carbonate (FEC, battery grade) [52]. For the conversion of LFMP to NFMP [41], LFMP was initially de-lithiated to FMP in a two-electrode Swagelok-type Li-cell by charging at the constant current rate of C/10 (1 C = 170 mA g^{-1}) from the OCV (~3 V) to 4.6 V, and holding the upper voltage limit until the current reached the limit of C/100 rate to ensure the complete FMP formation. The cell was then disassembled, the electrode collected and washed with DMC solvent, dried for 30 minutes under vacuum, and coupled with sodium metal disk in a new Na-cell. The electrochemical formation of NFMP was subsequently achieved by discharging the Na-cell until 1.8 V at a constant current of C/20 (1 C = 154 mA g^{-1}). The NFMP electrode was then recovered, washed with DMC solvent, and dried 30 minutes under vacuum before use. Additional coin-type control cells with the symmetrical configurations Na/Na, Li/Li, NFMP/NFMP, and LFMP/LFMP were assembled. For all the cells the applied current and the resulting capacity were calculated from weight of the pristine LFMP electrodes. All cells were assembled in argon-filled glove box (MBraun or Jacomex GP-Campus, with H_2O and O_2 content lower than 1 ppm).

2.4. Electrochemical Tests and ex-situ measurements

The electrochemical process features and the interphase characteristics of the

NFMP in sodium cell were investigated by coupling cyclic voltammetry (CV) and electrochemical impedance spectroscopy (EIS) at the room temperature (25 °C). Three-electrode Swagelok-type Na|NFMP cells were subjected to CV with a scan rate of 0.05 mV s^{-1} in the 1.8 – 4.3 V vs. Na^+/Na potential range, and the corresponding EIS responses collected after NFMP formation as well as after 1, 5, and 10 CV cycles at the bias potential of 1.8 V vs. Na^+/Na, by applying an alternate voltage signal of 10 mV in the 200 kHz – 100 mHz frequency range, with 10 points per decade and logarithmic spacing. The EIS spectra were analyzed through the non-linear least squares (NLLS) fitting method using the RelaxIS3 software (only fits with χ^2 values of the order of 10^{-4} or lower were considered) [53,54]. An additional CV test was performed within the same potential limits, by lowering the scan rate to 0.02 mV s^{-1} to achieve higher peak-resolution. Galvanostatic cycling tests for determining the battery performances of NFMP were conducted at the room temperature (25 °C) using two-electrode Na|NFMP cells. A rate capability test was performed by increasing the current rate from C/20 (1C = 154 mA g^{-1}) to C/10, C/5, C/2, 1C and 2C every 5 cycles and lowering back to C/20 after 30 cycles, in the 1.8 – 4.3 V voltage range. A constant-current constant-voltage (CCCV) test was performed as strategy to improve the Na^+ extraction/insertion and get the maximum cell capacity by setting the current at C/5 from 1.8 V to 4.3 V, and holding the charge voltage at 4.3 V until a current value of ¼ of the initial C-rate was reached. Afterwords, XRD scans and SEM images of pristine, sodiated, and cycled electrodes were collected as above described. Additional galvanostatic cycling was performed at 55 °C, and at temperature increasing from 45 °C to 50 °C, 55 °C, and 60 °C every 10 cycles at C/5 current rate in the voltage range of 1.8 – 4.3 V, by using the CCCV mode at 4.3 V during charge. Linear sweep voltammetry (LSV) was performed using three-electrode T-type cells with SP-Al electrode and EC:PC 1:1 v/v 1 M $NaPF_6$ + 2% FEC w/w as electrolyte at 25 °C, 50 °C, and 65 °C, with a scan rate of 0.1 mV s^{-1} from the OCV condition of the cells to 5.5 V vs. Na^+/Na. The diffusional features of Li^+ and Na^+ ions were investigated in comparison using CV, galvanostatic intermittent titration technique (GITT), and staircase electrochemical impedance spectroscopy (SPEIS) experiments. CV and GITT were performed using three-electrode Swagelok-type Na|NFMP and Li|LFMP cells, while SPEIS using coin-type cell. The CV tests were conducted at scan rates of 0.05, 0.10, 0.15, and 0.20 mV s^{-1} in the potential ranges 1.8 – 4.3 V vs. Na^+/Na for NFMP and 2.0 – 4.6 V vs. Li^+/Li for LFMP. GITT experiments were performed after three activation galvanostatic cycles performed at 0.05 current rate for NFMP (1C = 154 mA g^{-1}) and at 0.1 current rate for LFMP (1C = 170 mA g^{-1}), in the potential ranges of 1.8 – 4.3 V and 2.0 – 4.6 V for NFMP and LFMP, respectively. The titrations were carried out by applying current pulses of 7.7 mA g^{-1} for t = 2107.5 s for NFMP and of 17 mA g^{-1} for t = 1249.5 s for LFMP, followed by potential relaxation steps of 1 h at the open circuit. The GITT operating conditions, in terms of pulse magnitude and duration, have been decided basing on the galvanostatic cycles. SPEIS measurements were performed on both Li|LFMP and Na|NFMP two-electrode cells within one full cycle (3rd cycle) at different states of charge (SoC), during de-lithiation/de-sodiation and lithiation/sodiation, with a sampling interval of about 40

mV. For the measurements, an alternate voltage perturbation of 10 mV was applied within the 200 kHz – 10 mHz frequency range, with 10 points per decade and logarithmic spacing. The calculation of the distribution function of relaxation times (DRT) was performed after subtraction of the low-frequency diffusion region. The fitting procedure through the NLLS method [53,54] and the calculation of the DRT function were performed by using the software RelaxIS3. The optimization of the λ-factor for the DRT analyses was performed according to Tikhonov regularization by calculating the Sum of Squared Residuals (SSR) vs. λ, assuming a Gaussian distribution [55,56]. In order to separate the contributions of Li and Na counter electrodes from the Li|LFMP and Na|NFMP half-cell responses used for the DRT function calculation, and to assess at the same time the dependency of the charge transfer process on temperature, additional EIS measurements were performed on symmetrical Li|Li, Na|Na, LFMP|LFMP and NFMP|NFMP control cells at 5 °C, 15 °C, 25 °C and 35 °C. The CV, EIS and GITT measurements were carried out by using a VMP-3 multichannel electrochemical workstation with an integrated frequency response analyzer (Bio-Logic), while the cycling tests were performed by using a MACCOR series 4000 battery test system.

3. Results and discussion

3.1. Electrochemical conversion to NFMP

The electrochemical behavior during LFMP to NFMP conversion, and the related structural changes detected by XRD and Raman spectroscopy are illustrated in Fig. 1, while the corresponding morphological modifications are shown in Fig. S1 (Supplementary material). The voltage profile of Fig. 1(a) well reflects the de-lithiation of LFMP to FMP in a Li|LFMP cell, and the subsequent sodiation of FMP to NFMP in a Na|FMP cell (see experimental section for details on cell assembly and operating conditions). The de-lithiation (red line in Fig. 1a) proceeds with the expected shape, characterized by two plateaus at an average voltage of 3.5 and 4 V, ascribed to the Fe^{2+}/Fe^{3+} and Mn^{2+}/Mn^{3+} redox couples, respectively, with a delivered capacity close to the theoretical value. The data also evidence the conversion of FMP to NFMP with a capacity of about 140 mAh g^{-1}, which reflects 91% of the theoretical value, however with a slopping voltage (blue line in Fig. 1a) possibly affected by capacitive effects associated with the poor electronic and ionic conductivity of the FMP phase [57]. It is worth noting that the sodiation process reflects the solid-solution behavior at about 3.0 V vs. Na^+/Na associated with the Fe^{3+}/Fe^{2+} redox couple with the expected magnitude, as already reported for mixed olivines [45] and pure $NaFePO_4$ [58], and the sloped process of the Mn^{3+}/Mn^{2+} redox couple at about 3.5 V vs. Na^+/Na with a lower magnitude than that expected by the material stoichiometry. The lower activity of the latter redox couple compared to the former one is ascribed to the expected hindered kinetics and poor Na diffusivity in the manganese region compared to the iron one, mainly due to relevant Jahn-Teller distortion [27,46] and to possible Na/Mn antisite mixing that can lead to cation disorder and to partial formation of the natrophilite structure [39]. Nevertheless, the

figure. evidences a slight increase of the Fe^{2+}/Fe^{3+} redox potential in the mixed olivine compared with the one exclusively based on Fe, which is promoted by the presence of Mn as already observed in literature [46,59]. Structure, morphology, and composition of the pristine LFMP, the FMP intermediate, and the NFMP material are investigated by using electrodes collected from the corresponding cells at the SoC indicated by circles in Fig. 1(a) (see experimental section for details). The corresponding SEM images and EDS elemental maps reported in Fig. S1 reveal the presence of agglomerates of micrometric secondary particles, formed by sub-micrometric primary particles homogeneously blend into the electrode film, fully in line with the morphology of LFMP powder observed in previous paper [24]. The achievement of the conversion is supported by the experimental and reference diffractograms for LFMP (ICSD #166750) [49], FMP (ICSD #166750) [50], and NFMP (ICSD #26006) [51] in Fig. 1(b), which shows indexable crystalline structure for all the samples with negligible additional peaks, except for the one at ~44.7° attributed to the aluminum current collector [60]. Moreover, the figure indicates a limited amount of LFMP residue in the FMP electrode (arrow in the corresponding diffractogram), thus suggesting a relevant de-lithiation degree in agreement with the electrochemical profile [50]. To further investigate the structural features of the samples, Fig. 1(c) reports a Rietveld refinement of the diffractograms related with electrodes prepared with a high-loading to avoid the presence of Al current collector peak. The experimental XRD patterns (black dots) show that all the samples are characterized by an orthorhombic cell unit of the olivine lattice (*Pnma* space group, table N. 62) without significant impurities, as indeed confirmed by the refined diffractograms (red line) and the almost flat difference profile (blue line) [49,50]. The refinement results reported in Table 1 indicate for all the samples a goodness-of-fit parameter (*GOF*) <1.5 and a weighted-profile *R* factor (R_{wp}%) <15, thus suggesting an acceptable quality [61]. Indeed, R_{wp}% values higher than 10 are typically associated with XRD measurements carried out on electrode films, in particular upon cycling in cell. This condition can increase the noise of the diffractograms, and consequently the expected square variance factor (R_{exp}) which is strictly correlated with the R_{wp} [48,62]. Furthermore, the relevant number and the sharpness of peaks in the diffractograms can affect the R_{wp}% values [48]. Nevertheless, the graphical matching of the experimental points with the refined ones with modest differences (see Fig. 1c), the low values obtained for the *GOF*, and R_{wp}% values below 15 despite the phase complexity can confirm the reliability and the accuracy of the study [48,61]. The table also reveals values of the unit cell parameters (*a*, *b*, *c*) respectively of (10.3, 6.0, 4.7 Å) for LFMP, (9.7, 5.9, 4.8 Å) for FMP, and (10.5, 6.3, 5.0 Å) for NFMP [17,36]. These values are compatible with those of the reference diffractograms, and reflect in addition the bigger size of Na in NFMP compared with Li in LFMP, as well as the absence of the alkaline ion FMP structure [36,50]. Hence, the data show a decrease of the cell volume from ~295.6 $Å^3$ for LFMP, which exceeds the reference one in Table 1 in view of the higher Mn content, to ~267.0 $Å^3$ for FMP as the Li^+ is extracted, and a relevant increase to ~326.4 $Å^3$ in NFMP due to the large Na^+ insertion [49–51]. The values achieved for FMP and NFMP are comparable with those of heterosite and

triphylite structures, respectively, thus suggesting the formation of the desired structures during the electrochemical conversion process [36]. A further insight on the structural features of LFMP, FMP, and NFMP is achieved by Raman spectroscopy and related peak indexing in Fig. 1(d). All samples present the characteristic D and G bands of the carbon that coats the electrodes at 1350 and 1600 cm^{-1}, the peaks ascribed to the symmetrical and asymmetrical stretching of the phosphate PO_4^{3-} group with A_g mode centered at ~950 and ~1000 cm^{-1}, and the other peaks due to the symmetrical and asymmetrical bending of the PO_4^{3-} group with A_{2g} and B_{2g} modes at about 500 and 600 cm^{-1} [63,64]. The most relevant difference between the spectra is observed for the peak centered at about 450 cm^{-1} (highlighted region in Fig. 1d), associated with lithium or sodium cage modes with translating Li^+ or Na^+ and breathing cage surrounded by O^{2-} ions [63]. As expected, this peak is almost absent in the FMP spectra, while it is more intense and resolved in the NFMP spectra compared with LFMP one [41,63]. Further differences can be observed in the region between 50 and 300 cm^{-1}, which corresponds to the translational motions of the transition metals and the coupled translation-vibrational motion of the MO_6^- network bending [63,64]. Table 2 reports the results of the ICP-OES analysis on the LFMP, FMP, and NFMP electrodes, which confirm the success of the de-lithiation and subsequent sodiation process. The table shows sodium traces in LFMP and FMP samples which could be ascribed to possible contamination of the chemicals used for used for aqua regia preparation with the aim of dissolving the sample (see experimental section). Furthermore, the small lithium fraction detected in the de-lithiated and sodiated phases (i.e., ~5%) is in agreement with the small residual peak observed in the diffractograms (see Fig. 1b), thus confirming the above mentioned predominant de-lithiation/sodiation degree of the sample [50]. In summary, LFMP, FMP, and NFMP display well defined morphology and structure, and the data evidence a successful de-lithiation/sodiation process. These optimal characteristics, and the uniform distribution of the elements are crucial parameters to enable suitable interphase and satisfactory performance of the NFMP in sodium-cell [58].

Journal Pre-proofs

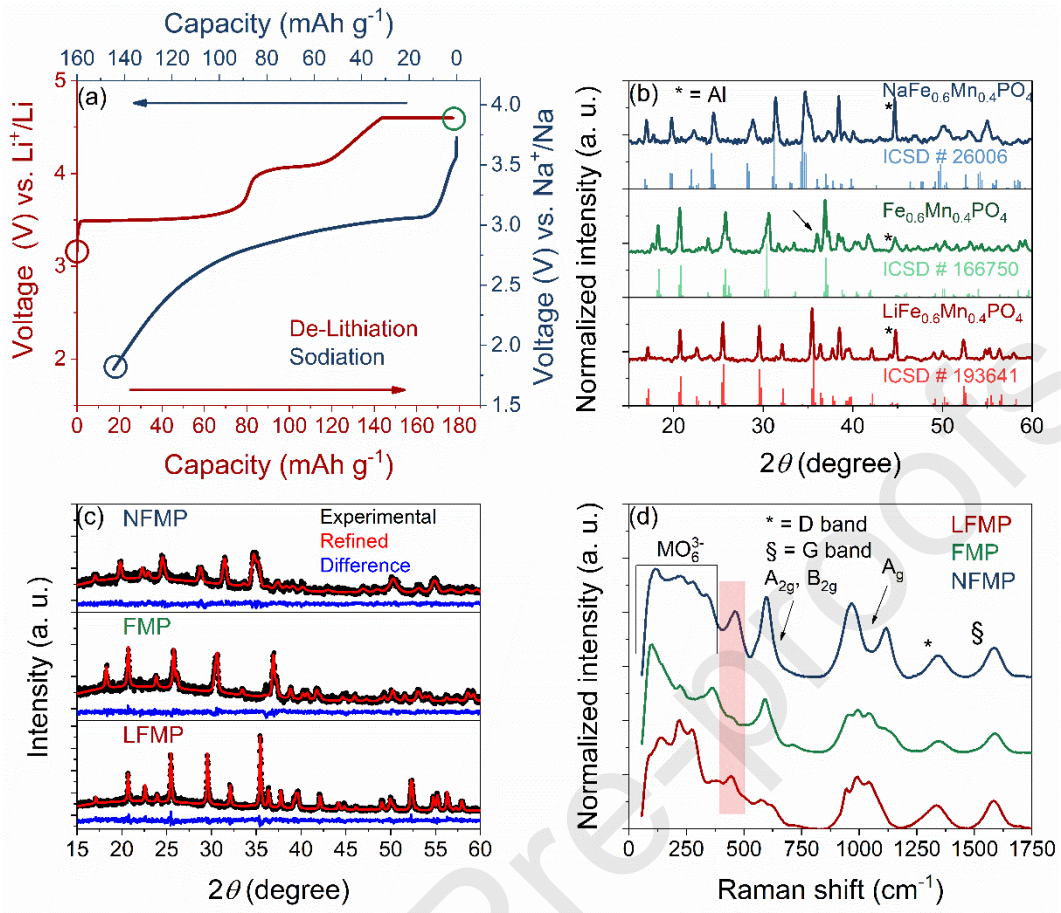

Fig. 1. Conversion of LFMP to NFMP. (a) Galvanostatic voltage profiles during de-lithiation of LFMP in Li-cell (red, left-hand *y*-axes, bottom *x*-axes) performed at C/10 (1C = 170 mA g^{-1}), and during subsequent sodiation of FMP in Na-cell (blue, right-hand *y*-axes, top *x*-axes) at C/20 (1C = 154 mA g^{-1}); circles indicate the state-of-charge of the electrodes corresponding to the subsequent ex-situ XRD study. (b) XRD patterns of the pristine LFMP electrode (red), de-lithiated FMP electrode (green), and sodiated NFMP electrode (blue) compared to corresponding reference diffractograms (ICSD #193641, ICSD #166750, and ICSD #26006, respectively). (c) Rietveld refinement of the XRD patterns (*Pnma* space group, N. 62) of LFMP, FMP, and NFMP electrodes. In detail: experimental (black dots) and calculated (red line) patterns, difference profile (blue line). (d) Raman spectra recorded in the 0 – 1750 cm^{-1} range. Highlighted region and indexing report transition identification. See the experimental section for details and the sample's acronym.

Table 1. Results of Rietveld refinement of the XRD patterns of Fig. 1(c) in terms of lattice parameters, unit cell volume, goodness-of-fit (*GOF*) parameter, and weighted-profile *R* factor (R_{wp}%) of LFMP, FMP, and NFMP, respectively. References: ICSD #193641 (LFMP); ICSD #166750 (FMP); and ICSD #26006 (NFMP). See experimental section for acronyms.

Sample	*a* (Å)	*b* (Å)	*c* (Å)	V (Å^3)	GOF (σ)	*R*wp%
ICSD #193641	10.343	6.022	4.704	293.03	–	–
LFMP	10.377(3)	6.044(5)	4.712(9)	295.61(9)	1.26	12.36
ICSD #166750	9.657	5.879	4.775	271.15	–	–
FMP	9.613(9)	5.839(1)	4.757(9)	267.09(2)	1.26	12.47
ICSD #26006	10.523	6.312	4.987	331.24	–	–
NFMP	10.446(1)	6.251(4)	4.997(5)	326.35(0)	1.20	11.75

Table 2: Results of ICP-OES measurements in terms of Li, Na, and P concentration and ratio between the alkali metals and phosphorus. See experimental section for acronyms.

Sample	Li concentration (ppm)	Na concentration (ppm)	P concentration (ppm)	Li/P ratio	Na/P ratio
LFMP	0.557	0.007	0.566	0.984	0.012
FMP	0.016	0.008	0.268	0.059	0.029
NFMP	0.018	0.400	0.425	0.042	0.941

3.2. Electrochemical Characterization of NFMP

The electrochemical process of the NFMP cathode is investigated in sodium cell by combining CV, EIS, and galvanostatic cycling as reported in Fig. 2. The CV response (Fig. 2a) shows during the first cycle two oxidation peaks centered at 3.1 V and 3.9 V vs. Na^+/Na and three reduction peaks centered at about 3.55 V, 3.0 V, and

Journal Pre-proofs

2.8 V vs. Na^+/Na. Indeed, the peaks at 3.1 V, 3.0 V, and 2.8 V vs. Na^+/Na are ascribed to the Fe^{2+}/Fe^{3+} redox couple, whilst those at 3.9 and 3.55 V vs. Na^+/Na to the Mn^{2+}/Mn^{3+} one, with de-insertion of Na^+ from NFMP during the anodic scan, and its insertion back into the olivine structure during the cathodic scan [65]. Similarly to Li-based olivine cathodes, the electrochemical process attributed to the Fe^{2+}/Fe^{3+} redox couple in NFMP occurs at higher potential compared to bare $NaFePO_4$, while that of Mn^{2+}/Mn^{3+} evolves at lower values with respect to $NaMnPO_4$ [31,65,66]. The transition metal redox potentials shift typically observed in the mixed olivines can be attributed to changes in the ionic character and distance of the M – O bond promoted by substitution [46,67,68]. In particular, a modification in the covalency of the M – O bond and M – O – M interaction has been observed to modify the position of the M^{2+}/M^{3+} redox energy, hence directly influencing the corresponding redox potential [59,69]. It is worth noting that the voltametric profile of NFMP is different from the one expected for pure $NaFePO_4$ [70], since it shows the presence of a multiple peak ascribed to Fe^{3+}/Fe^{2+} during sodiation instead of a single one, which is relevantly convoluted during de-sodiation process. Furthermore, the peak associated with the Mn^{2+}/Mn^{3+} shows a low intensity which further decreases after the first cycle during sodiation, thus suggesting an increase of the volume mismatch due to the high Mn content associated with the Jahn-Teller effect of Mn^{3+} [27]. The slow CV scan performed at 0.02 mV s^{-1} in Fig. S2 (Supplementary material) increases the peak resolution, and facilitates their association with the processes of the various redox couples. Indeed, the oxidation of Fe^{2+} to Fe^{3+} evolves during charge by a single-phase de-sodiation until $1 \leq x \leq 0.6$ in Na_xFePO_4 (anodic peak indexed as Fe^A in Fig. S2), and a two-phase reaction including both sodiation and Na^+/vacancies ordering for $x <$ 0.6 (anodic peak-shoulder indexed as Fe^B in Fig. S2). Despite the insertion process associated with LFP is mainly described as a two-phase reaction in literature [58,70,71], an intermediate phase cannot be completely excluded even for this material. On the other hand, NFP clearly presents two consecutive voltage peaks upon charge at about 2.95 and 3.11 V vs. Na^+/Na, merged into a single voltage peak upon discharge at about 2.8 V vs. Na^+/Na. This trend is certainly ascribed to a three-phase reaction mechanism, where an intermediate phase is foreseen in particular during the charge process [58]. The above described peak-split for the Fe^{3+}/Fe^{2+} couple, observed also during reduction however with a higher degree complexity, can be ascribed to the increase of the redox potential of a fraction of Fe promoted by the higher electronegativity of the Mn neighbor [45,46]. Furthermore, the first cycle of Fig. 2(a) (dark blue line) reveals a slightly higher polarization than the subsequent ones, thus suggesting an activation process mostly attributed to a partial structural reorganization of the sample, together with the formation of an appropriate solid electrolyte interphase at the anode side and solid polymer interphase at the cathode side (SEI/SPI) [72]. The subsequent voltammetry cycles in Fig. 2(a) show a well reversible electrochemical process evidenced by the overlapping of the cycles. The SEI/SPI formation is investigated in Fig. 2(b) by EIS measurements after the sodiation step, as well as after 1, 5, and 10 CV runs of NFMP in Na-cell, while the related interphase resistance obtained by non-linear least squares (NLLS) analysis are reported in Table

3 [53,54] The Nyquist plots reflect the shape associated to a blocking-type behavior of the fully-discharged state of the cell (i.e., at 1.8 V vs. Na^+/Na) upon which the EIS is collected. Overall, the curves are characterized by the presence of a medium-high frequency semicircle due to the electrode/electrolyte interface, and a low frequency tilted line representing the cell geometrical capacity [23]. The EIS response can be represented by the equivalent circuit $R_e(R_iQ_i)Q_g$, including in series the electrolyte resistance (R_e), one or two parallel of constant phase/resistance elements (R_iQ_i) mainly accounting for the SEI/SPI formed at the electrodes or marginal charge transfer, and a final constant phase element related to the cell capacitance (Q_g), despite a Warburg type diffusion cannot be completely excluded [53,54]. The data shown in Table 3 indicate an overall value of the interphase resistance of about 500 Ω, which is higher than ones reported for lithium mixed olivines [24], however in line with that associated to sodium-metal interphase [73]. It is worth mentioning that this value is typically limited by adding sacrificial substrates such as FEC in the electrolyte [74], or by using glyme-based electrolytes [75–77]. Nevertheless, the resistance values undergo very limited variation upon the voltametric scans, thus suggesting the formation of a stable SEI/SPI, in addition to the above mentioned structural reorganization which may favor the reaction. The rate capability of NFMP is reported in terms of the voltage profiles (Fig. 2c) and cycling trend (Fig. 2d) by increasing the current from C/20 to 2C (1C = 154 mA g^{-1}). The cell shows at the various C-rates the voltage shape expected by taking into account the CV of Fig. 2(a), characterized by a solid-state region with three plateaus at an average voltage of 3.0, 3.2, and 3.8 V, associated with Fe^{2+}/Fe^{3+} (Fe^A and Fe^B) and Mn^{2+}/Mn^{3+} redox couples, respectively. Moreover, the profiles in Fig. 2(c) indicate an increase of polarization by raising the current due to the increase of the ohmic polarization, which leads to the decrease of the capacity from 80 mAh g^{-1} (i.e.,, about 52% of the theoretical value) at C/20 to about 33 mAh g^{-1} (22% of the theoretical value) at 2C. The cycling trend of Fig. 2(d) reveals that the pristine capacity is recovered by decreasing the current back to C/20 after the whole test, thus suggesting the stability of the NFMP cathode upon the stress on the material structure triggered by the raising the current [31]. It is worth nothing that the first charge after the sodiation of the electrode at the same current (Fig. 1a) is characterized by a capacity of about 110 mAh g^{-1} (i.e., about 71% of the theoretical value), which is lower than the one obtained in the previous step (i.e., about 140 mAh g^{-1}). The figure also evidences a very modest contribution of the Mn^{2+}/Mn^{3+} redox couple to the overall cell capacity even at the lower current rate (i.e., C/20). This behavior may be ascribed to the above mentioned Jahn-Teller distortion promoted by Mn in olivines with high manganese content (i.e., $y > 0.2$ in $NaMn_yFe_{1-y}PO_4$) [46], which can relevantly hinder the transport of the voluminous sodium ion, [45], promote the strain, and increase the potential hysteresis during oxidation/reduction, thus limiting the $Na_zMn_yFe_{1-y}PO_4$ solid solution stability and the performances of the material [46,78,79]. Besides, the complete oxidation of Mn^{2+} to Mn^{3+} requires higher voltages than the theoretical one, in particular with high Mn content, thus leading to possible degradation of the conventional electrolytes [52]. Moreover, the Na^+/Na insertion/extraction in the olivine lattice may be affected by the

split of the Fe^{2+}/Fe^{3+} redox potential promoted by the higher electronegativity of the Mn neighbor [45,46], while Na and Mn can undergo the above mentioned antisite cation mixing in the structure with possible formation of the electrochemically inactive natrophilite phase [39]. To investigate the Na/Mn antisite mixing, the crystallographic details and the atomic parameters of NFMP are obtained from Rietveld refinement in Fig. 1(c), and summarized in Table S1 (Supplementary Material). It is worth mentioning that the occupancies of M1 and M2 sites vary during the refinement to allow the antisite mixing, and the results of Table S1 indicate a cation disorder of about 8% for NFMP cathode, especially ascribed to Mn^{2+}, thus justifying in part the limited contribution of the Mn^{2+}/Mn^{3+} redox couple to the cell capacity [39,47,80]. A possible strategy to increase the Na^+ extraction/insertion capacity in the olivine lattice is represented by the use of the constant current/constant voltage (CCCV) mode for charging the cell [81]. Accordingly, we have performed a CCCV cycling test of NFMP in Na-cell at a constant C-rate of C/5, with a constant voltage-step at 4.3 V during charge (see experimental section for testing details). The related voltage profiles reported in Fig. 2(e) shows the increase of the maximum capacity compared to the rate capability test, i.e., from ~60 mAh g^{-1} to ~78 mAh g^{-1}. Furthermore, the related cycling trend in Fig**.** 2(f) evidences a coulombic efficiency of about 72% at the first cycle, which increases and ranges between 98% and 100% during the subsequent ones, with a capacity retention of ~87% after 50 cycles and ~68% after 120 cycles. It is worth nothing that the sudden capacity increase around the 20^{th} cycle with corresponding coulombic efficiency oscillation observed in Fig**.** 2(f) may be due to a partial activation of the material, which is possibly triggered by the improvement electrode wetting achieved during the time evolution. Furthermore, the decrease of the capacity observed at the end of the test may be ascribed to the limitation of the charge transfer kinetics promoted by the excessive growth of the SEI/SPI layer upon prolonged cycling, as indeed suggested by the SEM inset in Fig**.** 2(f) of the NFMP before and after the test [36]. A more detailed view of the structural and the morphological features of the NFMP electrode upon the above cycling test is reported in Fig. S3 (Supplementary material). The XRD patterns of the electrodes (Fig. S3a) exhibit a defined crystalline structure, in full agreement with the one observed in Fig. 1(b and c) for NFMP, without significant modification, thus accounting for a relevant stability of the olivine framework [51]. Moreover, the SEM images of the pristine (Fig. S3b and c) and cycled (Fig. S3d and e) electrodes show the above-described agglomerates of primary sub-micrometric particles without relevant change of the NFMP, with additional domains characterized by rough morphology ascribed to the formation of the SEI/SPI [24,82]. Overall, Fig. 2 indicates the stability of both structure and morphology of NFMP upon cycling and its suitability for sodium cells, and suggests further tuning of the material composition in terms of Fe to Mn ratio to further improve the delivered capacity.

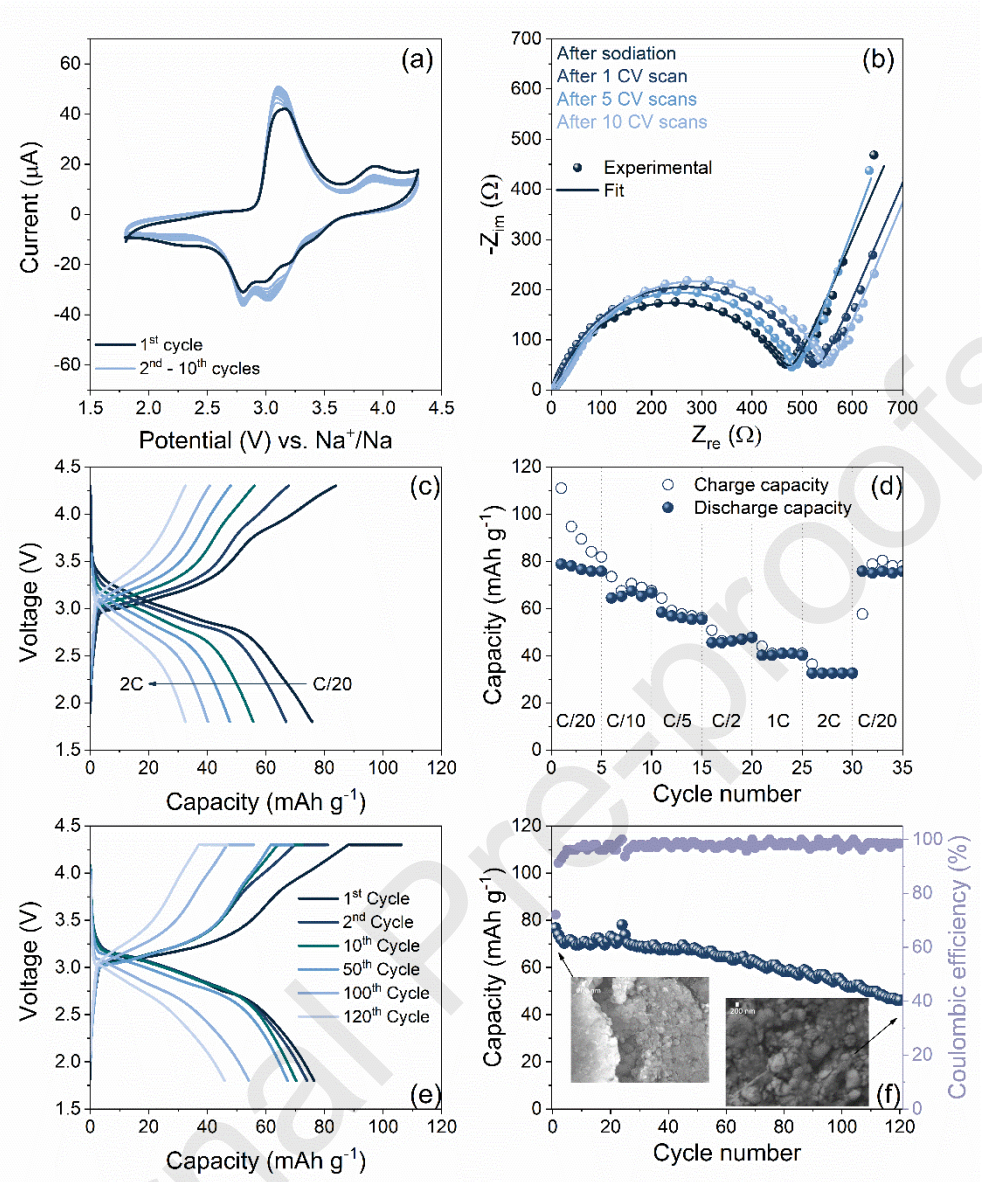

Fig. 2. Performance of NFMP in Na-cell at room temperature (25 °C). (a) CV profiles and (b) EIS measurements after sodiation of the electrode, and after 1, 5, and 10 voltammetry cycles. Potential range (3-electrode cell) 1.8 – 4.3 V vs. Na^+/Na; scan rate 0.05 mV s^{-1}; EIS frequency range 200 kHz – 100 mHz; alternate voltage signal amplitude 10 mV. (c) Voltage profiles and (d) cycling trend of the galvanostatic test performed at C/20, C/10, C/5, C/2, 1C, and 2C currents (1C = 154 mA g^{-1}). (e) Voltage profiles and (f) cycling trend of the prolonged galvanostatic test performed at the constant current rate of C/5 with discharge capacity in left-hand side *y*-axes and coulombic efficiency in right-hand side *y*-axes. Voltage range 1.8 – 4.3 V, with an additional constant voltage step at 4.3 V (CCCV mode) until a final current of ¼ referred to the nominal C-rate for the prolonged test at C/5. Inset in (f): SEM images of the NFMP electrode before and after cycling test. See the experimental section for acronyms.

Table 3. NLLS analysis of the Nyquist plots reported in Fig. 2(b) recorded by

performing EIS on a Na|NFMP three-electrode cell. NLLS fitting method was applied through a RelaxIS3 software and only fits with a χ^2 value of the order of 10^{-4} or lower were considered suitable. See experimental section for acronyms

Cell condition	Equivalent circuit	$R_{i,\,1}$ (Ω)	$R_{i,\,2}$ (Ω)	$R_{i,\,1} + R_{i,\,2}$ (Ω)	χ^2
After sodiation	$R_e(R_{i,\,1}Q_1)Q_g$	465 ± 2	–	465 ± 2	2 x 10^{-4}
After 1 cycle	$R_e(R_{i,\,1}Q_1)(R_{i,\,2}Q_2)Q_g$	5.1 ± 0.2	513.4 ± 1.2	518.5 ± 1.2	5 x 10^{-5}
After 5 cycles	$R_e(R_{i,\,1}Q_1)(R_{i,\,2}Q_2)Q_g$	19.1 ± 0.5	458.5 ± 1.4	477.6 ± 1.5	5 x 10^{-5}
After 10 cycles	$R_e(R_{i,\,1}Q_1)(R_{i,\,2}Q_2)Q_g$	30.6 ± 0.8	508.9 ± 1.7	539.5 ± 1.9	4 x 10^{-5}

The increase of the Na^+ ion mobility in the olivine framework against the distortion and strain triggered by the Mn^{2+}/Mn^{3+} redox couple at 3.8 V may be actually promoted by increasing the temperature according to the Arrhenius trend. The above improvement of the material conductivity, which may also fasten the reaction kinetics, is typically reflected into a linear increase of the cell capacity by raising the temperature [38,83]. Hence, Fig. 3 reports the galvanostatic cycling of the NFMP cathode in sodium cell performed at C/5 rate (CCCV mode), increasing the temperature by 5°C every 10 cycles from 45 °C to 60°C. The voltage profiles of Fig. 3(a) selected at 45 °C, 50 °C, 55 °C, and 60 °C present the solid-state region with three plateaus with average voltage of 3.0, 3.2, and 3.8 V previously described, and associated to the Fe^{2+}/Fe^{3+} and Mn^{2+}/Mn^{3+} redox couples, respectively. It is worth noting that the increase of the temperature leads to the desired raise of the capacity provided by the cell from about 80 mAh g^{-1} at 45 °C to about 110 mAh g^{-1} at 60 °C, with a high stability and efficiency for the tests performed at 45 °C, 50 °C and 55 °C according to the trends in Fig. 3(b). The activation already observed at 25 °C may be also promoted by temperature increase, according to the gradual trend observed in Fig. 3(b) at 45 °C and 50 °C. However, the reason for improvement in this case may be found in the increase of the material conductivity following the Arrhenius trend [73]. The maximum capacity of the cell is reported in Fig. 3(c) as a function of the temperature, and plotted as a line with a relevantly high confidence (R^2 = 0.9994). The

achieved trend well accounts for the above mentioned effect of the increase of Na^+ ions conductivity into the material framework triggered by the temperature. Despite the test performed at 60 °C achieves the highest value, it also reveals a progressive decrease of the cell capacity and coulombic efficiency, as expected by the more relevant effect of the electrolyte decomposition and electrode/electrolyte interphase excessive growth promoted by the higher temperature [83–85]. To investigate the possible electrolyte oxidation at increased temperature, the anodic electrochemical stability window (ESW) is measured by LSV at 25 °C, 50 °C, and 65 °C and the results are shown in the inset Fig. 3(c) (see experimental section for the related cell setup). The data reveal the complete stability of the electrolyte at 25 °C in the 1.8 – 4.3 V vs. Na^+/Na voltage range, which is the interval used for cell cycling. Indeed, the full oxidative decomposition of the electrolyte is detected above 5 V vs. Na^+/Na at 25 °C. However, the increase of the temperature limits the ESW of the electrolyte to ~4.5 V vs. Na^+/Na at 50 °C, and below 4.2 V vs. Na^+/Na at 65 °C. These results confirm the possible electrolyte decomposition at the higher temperatures that can lead to decrease of the cell capacity and coulombic efficiency [84,85]. Nevertheless, the interphase stability below 65 °C suggests the relevant compatibility of the electrolyte with the NFMP electrode, as also indicated by the formation of a stable SEI/SPI (see Fig. 2b and Table 3). Therefore, the temperature of 55 °C is chosen as a suitable compromise between delivered capacity, high coulombic efficiency, and good retention. Accordingly, Fig. 3(d) reports the galvanostatic voltage profiles of the Na|NFMP cell at 55 °C, while Fig. 3(e) depicts the corresponding cycling trend. The cell shows the plateaus associated with Fe^{2+}/Fe^{3+} and Mn^{2+}/Mn^{3+}, where the plateau at 3.8 V associated with the latter redox couple presents a more defined shape (Fig. 3d), thus suggesting a mitigated effect of the Jahn-Teller distortion [27]. Furthermore, the cell reveals a maximum specific capacity of about 100 mAh g^{-1}, a coulombic efficiency of about 78% at the first cycle which increases and ranges from about 97% to 99% during the subsequent ones, with a capacity retention of about 75% after 50 cycles (Fig. 3e).

Journal Pre-proofs

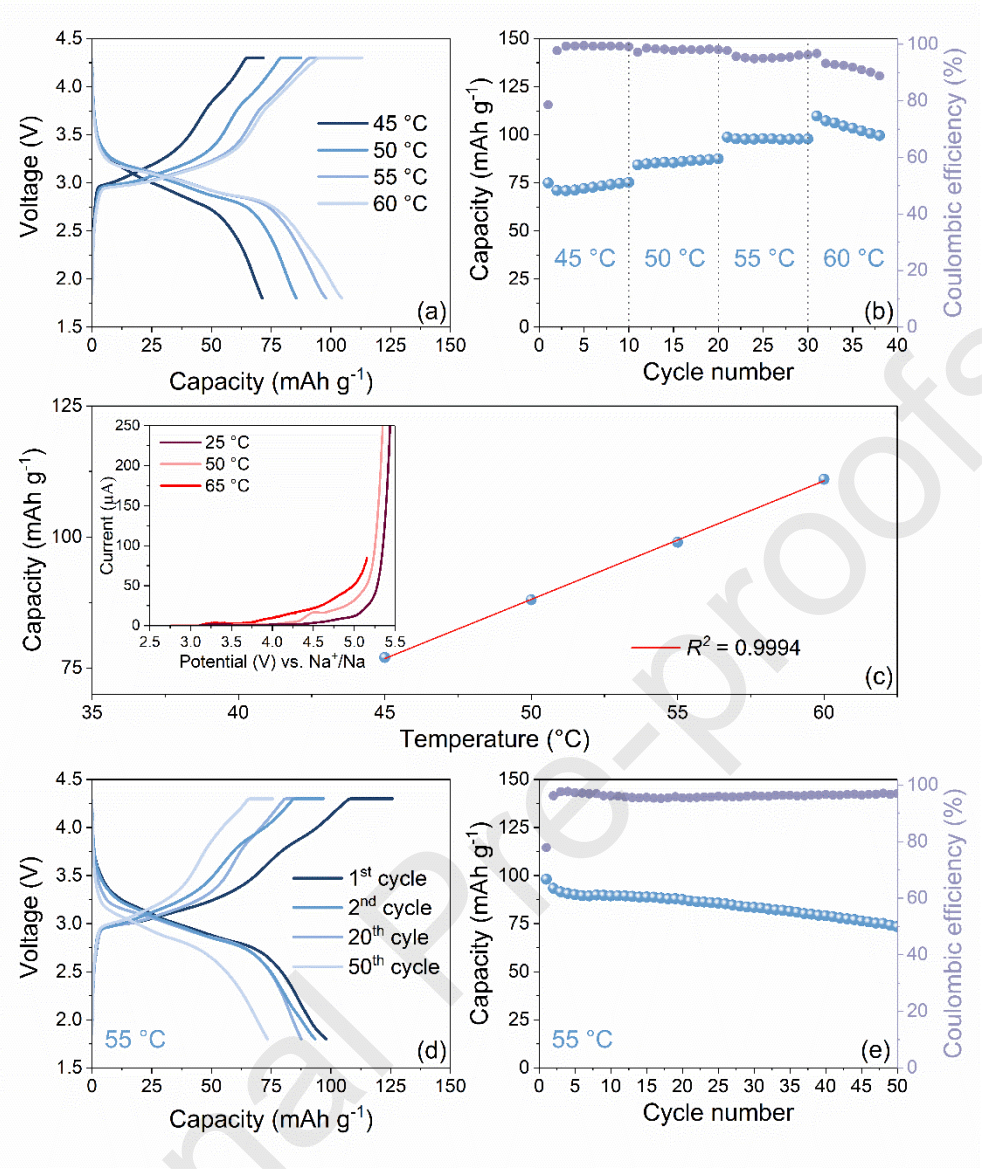

Fig. 3. Performance of NFMP in Na-cell at various temperatures. (a) Voltage profiles and (b) cycling trend of the galvanostatic test performed at C/5 current rate (1C = 154 mA g^{-1}) by changing the temperature from 45 °C, 50 °C, 55 °C, and 60 °C. (c) Linear trend of the maximum specific capacity delivered by NFMP vs temperature. Inset in (c): LSV measurements of the Na|EC:PC 1:1 v/v 1 M $NaPF_6$ + 2% FEC w/w|SP-Al cells for determining the anodic electrochemical stability window (ESW) of the electrolyte at 25 °C, 50 °C, and 65 °C. Scan rate 0.1 mV s^{-1}. (d) Voltage profiles and (e) cycling trend of the galvanostatic test performed at C/5 current rate (1C = 154 mA g^{-1}) at the constant temperature of 55 °C with discharge capacity in left-hand side *y*-axes and coulombic efficiency in right-hand side *y*-axes. Voltage range 1.8 – 4.3 V with an additional constant voltage step at 4.3 V (CCCV mode) until a final current of ¼ referred to the nominal C-rate. See the experimental section for acronyms.

Overall, the temperature has a beneficial effect on the performances of the cell, which reaches higher capacity, a more defined process associated with the transition

metal redox couples without significant strain transformation, and a good coulombic efficiency. Nevertheless, the lower retention and the slightly lower coulombic efficiency compared to the cell cycled at 25 °C (i.e., 87% respect to 75% after 50 cycles and 97% compared to 100%, respectively) suggest a modest decomposition of the electrolyte at 55 °C as discussed above [85] and the necessity of *ad hoc* tuned electrolyte with a better anodic stability, as well as further improvement of the NFMP electrode to achieve higher performance and stability [24,58,86].

3.3. Ion transport and interphase properties of LMFP and NFMP

The understanding of thermodynamics and kinetics plays key role for evaluating the cycling performances, the ions diffusion and the interfacial properties of mixed olivines [87]. Although olivine NFMP has the same phase structure as olivine LFMP (see Fig. 1), they intrinsically differ by the electrochemical process [41,47,68]. According to the data illustrated above (see Figs. 2 and 3), we may speculate that the typical phase transformation and ion transport kinetics in NFMP are clearly worse during the (de)insertion of Na^+ in NFMP compared with the analogue LFMP [24]. To further shed light on this aspect and properly evaluate the electrode behavior in sodium cell, we perform hereafter a comparative investigation between NFMP and LFMP. In particular, we evaluate the difference in the Li^+ or Na^+ ions diffusion coefficient, the equilibrium potential of the ion insertion/extraction, and the charge-transfer kinetics of the two materials. It is worth mentioning that the ion transfer occurring at the electrode/electrolyte interphase can be influenced by the different electrolyte media (e.g., EC/DMC for lithium and EC/PC for sodium batteries). On the other hand, the impact of the different solvents on the ion migration at the interphase is already demonstrated using various combinations of substrates and electrolytes, including the carbon-based electrodes in the EC/DEC or EC/EMC media [84,86]. Salt chemistry may also have a concomitant role together with solvent in driving the performances of the Na-battery in terms of ion transport and conductivity. Hence, sodium hexafluorophosphate in the EC:PC solvent has been proven to outperform in SIBs the conventional EC:DMC mixture typically used in LIBs, leading to higher capacity retention and coulombic efficiency. However, this improvement is typically much more relevant at the anode side, where a thick electrolyte interphase (SEI) can be formed [72]. Thickness, composition and stability of the SEI at the SIBs anode is indeed ascribed to the electrolyte stability towards reduction at low potentials, and it can severely affect the ion transfer [88]. This effect is less pronounced at the cathode side since SIBs typically operate below the electrolyte oxidation limit. Therefore, the surface layer formed at the higher potentials by marginal oxidation at the cathode surface is thin, in particular using EC:PC solvent mixture which displays enhanced anodic stability at room temperature [88]. Although, the comparable charge transfer resistance throughout the whole cycling of the two systems studied herein (LFMP and NFMP), despite the change of the electrolyte solution, well supports the above mentioned limited influence of the solvent mixture.

Fig. 4 depicts the CV responses at increasing scan rates of LFMP in Li-cell (Fig.

4a) and NFMP in Na-cell (Fig. 4b). The current peak values (I_p) increase by rising the scan rate (v), according with a linear trend of I_p vs. $v^{1/2}$, thus suggesting lithium or sodium diffusion as rate-determining step of the redox processes (see Fig. S4 in Supplementary material for the related plots). The measured values have been used to calculate the Li^+ and the Na^+ diffusion coefficients for LFMP and NFMP, respectively, D_{CV} ($cm^2\ s^{-1}$), according to the Randles – Sevcick equation (Eq. (1)) [89]:

$$I_p = 0.4463zFAC\sqrt{\frac{zF\nu D_{CV}}{RT}} = 2.686 \cdot 10^5 AC\sqrt{z^3\nu D_{CV}} \quad \text{with T = 298.15 K} \qquad (1)$$

where I_p is the peak current value (A), $z = 1$ is the number of exchanged electrons, F is the Faraday constant (96485 C mol^{-1}), A is the electrodes geometric area (0.785 cm^2), C is the Li^+ or Na^+ concentration within the olivine lattice (mol cm^{-3}), v is the scan rate (V s^{-1}), R is the gas constant (J K^{-1} mol^{-1}), and T is the temperature (K). The obtained values of the D_{CV} for LFMP and NFMP are shown in Fig. 4(c and d), respectively, and calculated by considering the I_p vs. $v^{1/2}$ linear slope of the Fe^{2+}/Fe^{3+} and Mn^{2+}/Mn^{3+} current peaks during charge and discharge processes, as illustrated in Fig. S4. It is worth mentioning that during NFMP sodiation process, only the peaks associated with the Fe^{2+}/Fe^{3+} redox couple (Fe^A and Fe^B) are taken into account, since the weakness of the peak associated with Mn avoids an accurate determination of D_{CV} [45]. The results of Fig. 4(c and d) indicate a much faster ion transport in LFMP compared to NFMP, with D_{CV} values above 10^{-10} $cm^2\ s^{-1}$ for the former and in the order of 10^{-12} $cm^2\ s^{-1}$ for the latter. Moreover, the D_{CV} values herein obtained for LFMP are slightly higher than the value already reported in literature for $LiFe_{0.5}Mn_{0.5}PO_4$ prepared by solvothermal reaction, thus indicating that the sol-gel synthesis could be a suitable choice for an enhanced structure [26,90].

Journal Pre-proofs

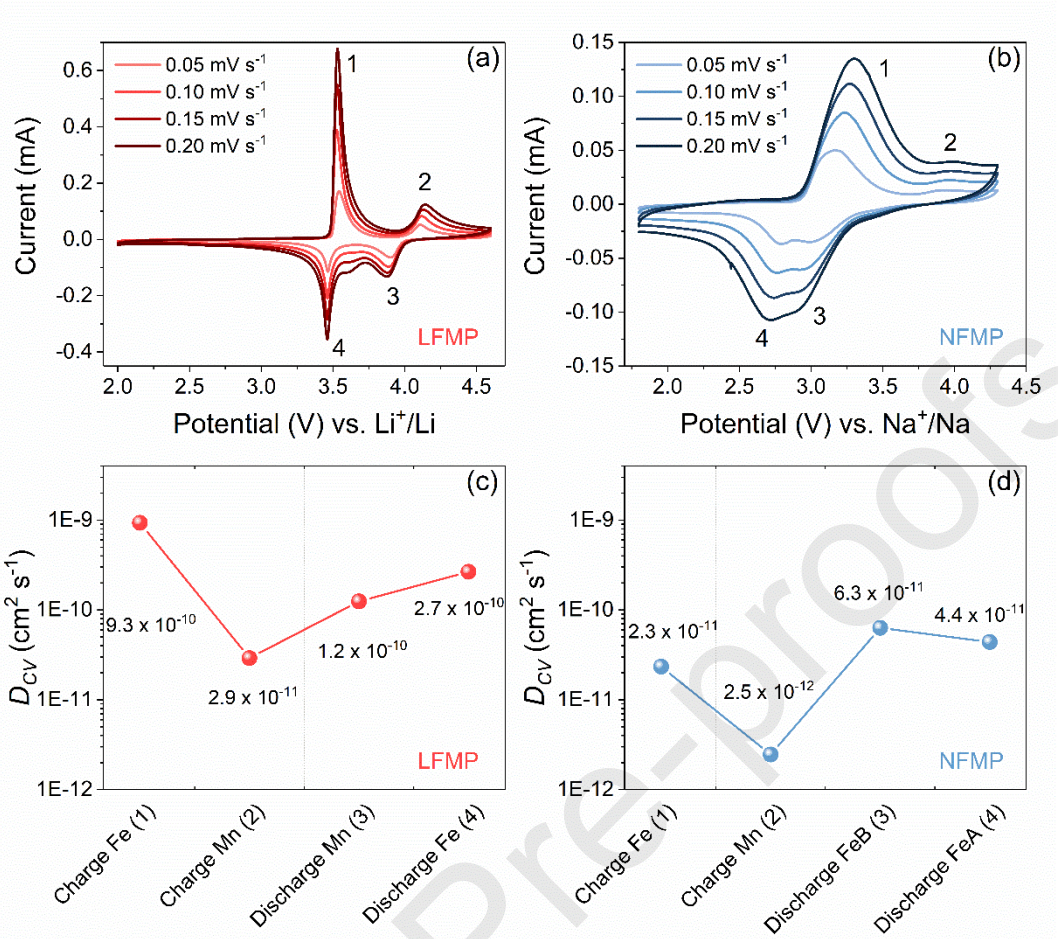

Fig. 4. Steady-state CV profiles with indexed peaks of (a) LFMP in Li-cell and (b) NFMP in Na-cell with 3-electrode setup at scan rates (v) of 0.05, 0.1, 0.15, and 0.2 mV s^{-1}. Potential range 2.0 – 4.6 V vs. Li^+/Li for LFMP and 1.8 – 4.3 V vs. Na^+/Na for NFMP. Trends of D_{CV} (diffusion coefficients from CV) at various SoC for (c) Li^+ in LFMP and (d) Na^+ in NFMP calculated using Eq. (1), taking into account the linear trend of Fe^{3+}/Fe^{2+} and Mn^{3+}/Mn^{2+} current peaks (I_p) reported in Fig. S4 (Supplementary material) versus the square root of the scan rates during oxidation and reduction processes. Room temperature (25 °C). See the experimental section for acronyms.

Nevertheless, the NFMP reported herein presents higher values of D_{CV} compared to the ones reported in literature for pure $NaFePO_4$, thus suggesting a concomitant effect of Na^+-(de)intercalation features and optimized synthesis on the transport properties [66,87]. The above trends also evidence for both LFMP (Fig. 4c) and NFMP (Fig. 4d) a decrease for 1 order of magnitude of D_{CV} by cell charging and its increase back by discharging, thus accounting for the remarkably lower ionic conductivity of the de-lithiated/de-sodiated phase of the olivine compared to the lithiated/sodiated one, that can be remarkably increased by a fine tuning of the carbon coating in the electrode [91].

Journal Pre-proofs

Further determination of Li^+ and Na^+ diffusion coefficients for LFMP and NFMP performed by GITT, is reported in Fig. 5, according to the method proposed by Weppner and Huggins [92]. Prior to GITT experiment, three galvanostatic cycles have been performed on LFMP and NFMP for limiting possible effects given by the stabilization of the interphase or the activation of the material, and the related voltage profiles are shown in Fig. S5 (Supplementary material). Fig. 5(a and b) show the time evolution of the potential during titration (black curves), obtained by applying repeated current pulses followed by potential relaxation steps in three-electrode lithium and sodium cells using LFMP and NFMP, respectively (see the experimental section for details). Small constant current of C/10 for LFMP and C/20 for NFMP are used during GITT in order to assume the diffusion process in the surface layer, as proposed by Weppner and Huggins [92]. The same panels show the overlap of the quasi-equilibrium potential profiles (E_0) during charge (dark red and dark blue) and discharge (light red and light blue) for LFMP and NFMP, respectively, after relaxation (see detailed examples of the potential evolution during a single GITT step obtained for LFMP and NFMP in Fig. S6 of Supplementary material). The trend of E_0 vs. x (exchanged lithium or sodium degree in $M_{1-x}Fe_{0.6}Mn_{0.4}PO_4$ olivine, with M = Li or Na) reveals a reversible titration extended up to $x = 0.69$ for LFMP (Fig. 5c) and to $x = 0.5$ for NFMP (Fig. 5d) under quasi-equilibrium conditions. The difference of the maximum value of x in NFMP and LFMP is ascribed to a more relevant strain in the olivine structure induced by the bigger Na^+ compared with Li^+, which is reflected into a slower ion diffusion kinetics, in particular in view of the above mentioned Jahn-Teller distortion promoted by Mn [46,90]. It is worth noting that the quasi-equilibrium potential hysteresis for NFMP (Fig. 5d) is around 120 mV, which is more than 4 times larger than that of LFMP (i.e., 30 mV, Fig. 5c) at the same alkali ion content. This behavior, already observed for $LiFePO_4$ and $NaFePO_4$, is related with a more relevant phase transitions stress due to the larger volume change between sodiated and de-sodiated olivine compared to lithiated and de-lithiated one [87]. The Li^+ or Na^+ diffusion coefficients, D_{GITT} ($cm^2\ s^{-1}$), are obtained using the data of Fig. 5 and applying Eq. (2):

$$D_{GITT} = \frac{4}{\pi}\left[\frac{I^0 V_M}{AF}\frac{dE/dx}{dE/dt^{1/2}}\right]^2, \quad t \ll \tau \qquad (2)$$

where I^0 (A) is the applied current, V_M is the olivine molar volume (44.53 $cm^3\ mol^{-1}$ for LFMP and 48.21 $cm^3\ mol^{-1}$ for NFMP), A is the electrode geometric area (0.785 cm^2), F is the Faraday constant (96485 C mol^{-1}), and τ is the diffusion time (s). dE/dx is determined by derivation of the titration curves in Fig. 5(c and d). $dE/dt^{1/2}$ is obtained by linear fit of E vs. $t^{1/2}$ related to each current pulse (with $t << \tau$, see examples of slope determination for current pulses related to $x = 0.55$ in $Li_{1-x}Fe_{0.6}Mn_{0.4}PO_4$ and to $x = 0.23$ in $Na_{1-x}Fe_{0.6}Mn_{0.4}PO_4$ in Fig. S6(c and d), respectively). Fig. 5(e) represents the D_{GITT} during de-lithiation/lithiation and de-sodiation/sodiation as function of the state of charge (x) for LFMP (red) and NFMP (blue). For the sake of clarity the values of D_{GITT} obtained for LFMP and NFMP for each GITT step are reported in Tables S2 and S3 (Supplementary

material), respectively, together with the corresponding quasi-equilibrium potential (E_0) and exchanged alkali ion degree (x). The results evidence the typical trend observed for mixed olivines with a general decrease of D_{GITT} for the de-lithiated/de-sodiated phases at high x [26], with higher values for LFMP compared with NFMP suggesting slower kinetic of Na^+ than Li^+, as already observed for D_{CV} in Fig. 4. In detail, Fig. 5(e) reveals an initial increase of D_{GITT} by charge to a maximum value of ~10^{-9} cm^2 s^{-1} at x = 0.42 for LFMP and ~10^{-11} cm^2 s^{-1} at x = 0.29 for NFMP, and a subsequent relevant decrease by further increasing x to a minimum value of ~10^{-13} cm^2 s^{-1} for LFMP and ~10^{-14} cm^2 s^{-1} NFMP.

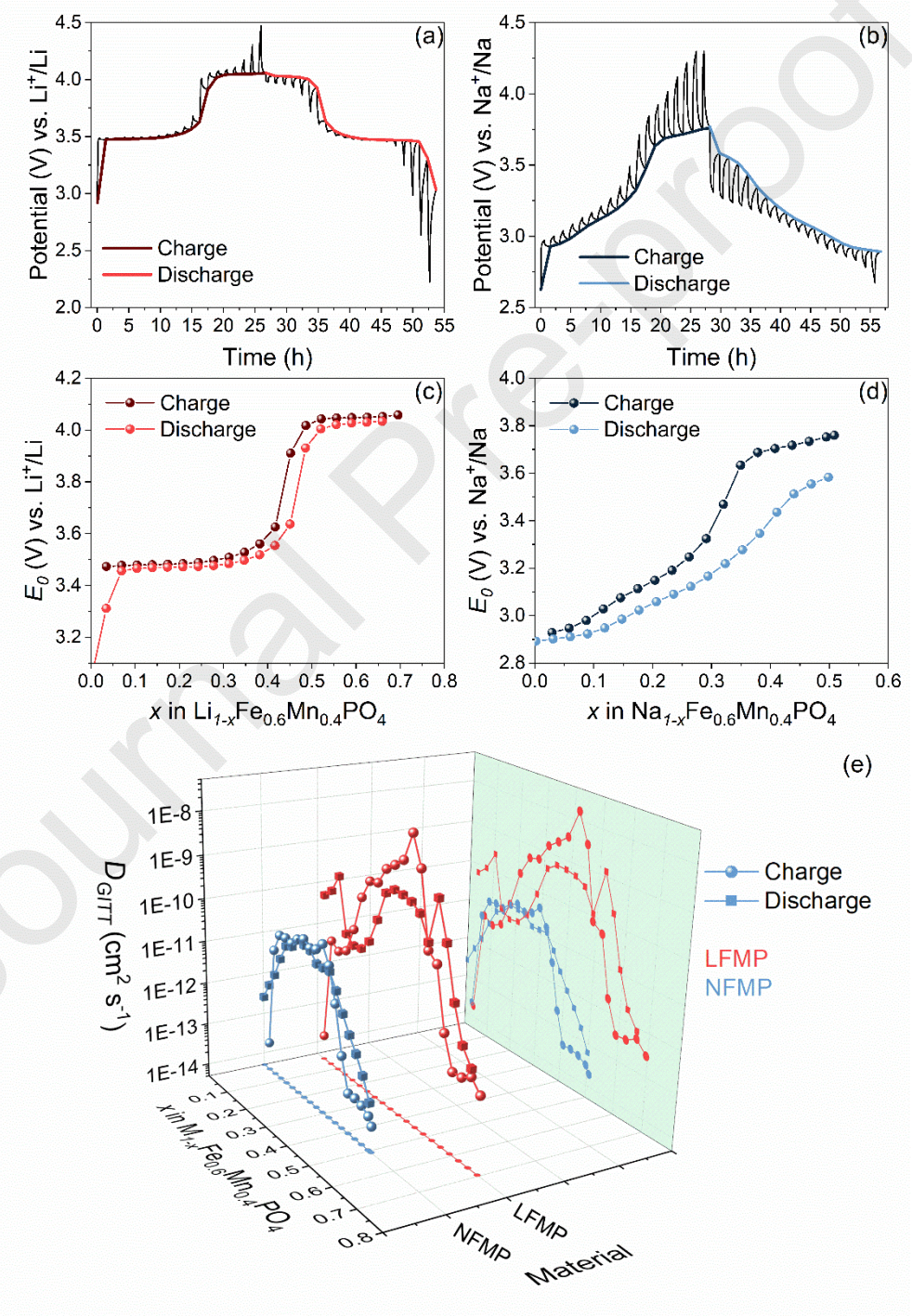

Journal Pre-proofs

Fig. 5. GITT curves in terms of E_0 (quasi-equilibrium potential after relaxation) vs. time of (a) LFMP in Li-cell and (b) NFMP in Na-cell with 3-electrode configuration, with overlapped black curves reporting the overall time evolution of the potential during current pulses and relaxation steps. Trends of E_0 vs. x (exchanged alkali metal degree) for (c) LFMP and (d) NFMP determined from GITT. (e) Three-dimensional representation of D_{GITT} (diffusion coefficient from GITT) vs. x for Li^+ ions in LFMP and Na^+ ions in NFMP calculated using Eq. (2). Applied pulses current: 17 mA g^{-1} (0.1 C rate) for LFMP and 7.7 mA g^{-1} (0.05 C rate) for NFMP. Potential range 2.0 – 4.6 V vs. Li^+/Li for LFMP and 1.8 – 4.3 V vs. Na^+/Na for NFMP. Room temperature (25 °C). See the experimental section for acronyms and Figs. S5 and S6 (Supplementary material) for the preliminary activation cycles and pulse detail, respectively.

It is worth noting that the diffusion coefficients during the discharge are smaller than the values during the charge, likely due to the insulating character of de-lithiated/de-sodiated olivine. Previous studies indicated much lower D for $LiFePO_4$ (LFP) and $NaFePO_4$ (NFP) compared to LFMP and NFMP, with values ranging from 10^{-17} to 10^{-13} cm^2 s^{-1} for lithium and from 10^{-19} to 10^{-15} cm^2 s^{-1} for sodium, depending on the x value as well as the experimental setup [66,87,93,94]. This discrepancy may be ascribed to the different Li^+/Na^+ (de)insertion mechanism in LFMP/NFMP compared with LFP/NFP, where the former foresees two or three interconnected *solid-solution-like* working regions, while the latter has a defined flat plateau [26,30,45,46]. Nevertheless, an intrinsic experimental error of the Li^+ and Na^+ diffusion coefficient determination from GITT data for two-phase materials, ascribed to the solid-solution assumption proposed by Weppner and Huggins, could not be excluded [92]. In particular, the Weppner model has been described to provide D values for $LiFePO_4$ and $NaFePO_4$ of about 3 orders of magnitude lower in the two-phase region compared with in the single-phase one [93,94]. This discrepancy could be ascribed to an intrinsic experimental error on Li^+/Na^+ diffusion coefficient determination triggered by the characteristic reaction mechanism of the olivines. It is worth mentioning that additional experimental parameters could affect the results of the GITT [95], such as time and number of the current steps, the relaxation time, as well as the electrode film features (i.e., uncertainty of surface area, reaction-limitation, inter-particle composition differences, finite size and non-planar geometry). On the other hand, systematic errors derived from composition-dependent overpotentials can be limited by minimizing the current magnitude to support the assumption of semi-infinite behavior also for finite-size spherical particles. In fact, this assumption in planar systems is suitable for very short diffusion time, such as the value adopted in this work ($\tau < 0.25$) which is optimized to achieve reliable D_{GITT} value [95]. In this respect, a computational study indicates that the underestimation of the diffusion coefficients in electrodes with flat-shaped potential using GITT can be strongly limited by lowering the thickness to get a more accurate D_{GITT} [96]. Overall, the D_{GITT} values obtained in Fig. 5(e) for LFMP and NFMP are comparable with the

ones obtained by CV (see Fig. 4), and with those achieved by GITT in other studies focusing on lithium diffusion in mixed olivines [26]. Despite slower ion transport and diffusion leading to a sluggish kinetics, Fig. 5 suggests that the NFMP cathode achieved by electrochemical conversion and the pristine LFMP have a surprisingly similar transport mechanism.

To further understand and compare the interfacial and charge-transfer kinetics of LFMP and NFMP, SPEIS experiments are performed by running impedance measurements at different SoC upon full de-lithiation/de-sodiation and subsequent lithiation/sodiation, and the related DRT functions are calculated [97–99]. The measurements are acquired during the 3rd cycle to minimize any bias arising from possible stabilizations of the interphases or activation of the materials, by using a two-electrode coin cell setup to avoid possible inductive contributions, given by the reference electrode. The Nyquist plots obtained upon LFMP (de-)lithiation in Fig. S7 (Supplementary material) display the presence of four main features: (I) an intercept to the real axis accounting for the electrolyte resistance; (II) a high-frequency semicircle accounting for particle-particle and particle-current collector contact resistance, with the associated double-layer capacitance; (III) a medium/low-frequency semicircle accounting for the interphase and charge-transfer sum resistance of both LFMP and Li metal electrodes, coupled to the related capacitances due to surface charge accumulation; (IV) a low-frequency line accounting for solid-state diffusion, changing shape from reflective to transmissive conditions according to the changes in the SoC [100]. As the calculation of DRT from EIS requires the solution of an ill-posed problem, Tikhonov regularization is here employed [56]. Specifically, the boundary conditions require the impedance spectra to converge towards the real axis, where the angular frequency ω tends to zero; however, this requirement is usually not encountered in typical EIS spectra, as the low-frequency diffusion region diverges from the real axis, and a pre-processing step for the Nyquist plots is required [55,56]. Hence, the raw spectra from Fig. S7(a and b) have been modeled, as a first approximation, to the equivalent circuit $R_e(R_iQ_i)WQ_w$, with particular attention to the fitting of the low-frequency region [53,54]. In the adopted model, R_e represents the electrolyte resistance (high-frequency intercept with the real axis), in series with three resistances and constant phase elements in parallel, $(R_iQ_i) = (R_1Q_1)(R_2Q_2)(R_3Q_3)$, and a Warburg element with a constant phase element (WQ_w). The above elements respectively account for the contact resistance between electrode particles and current collector (high-frequency semicircle), the interphase associated with the SEI/SPI, the charge transfer of the electrodes (medium- and low-frequency semicircles), and the solid-state diffusion (low-frequency tilted line). The fitted low-frequency region, as simulated by the WQ_w elements, is then subtracted from the overall impedance to obtain the convergence of the spectra to the real axis. Interestingly, the obtained Nyquist plots after removal of the diffusive part (Fig. 6a and c) show the appearance of a third semicircle in the low-frequency range, previously not visible due to the partial overlapping with the Warburg diffusion line. The fitted spectra in Fig. 6(a) display upon de-lithiation relatively constant intercept with the real axis and unchanged high-frequency semicircle, thus confirming the

stability of the electrolyte and the electrode slurry since the related resistances (R_e and $R_1 = R_{cont}$, respectively) are almost unaltered. On the other hand, a progressive decrease in the diameter of the semicircles at medium- and low-frequencies (R_2 and R_3) is encountered by lithium extraction up to 3.5 V, with a slight increase after 4.2 V (see fitted values in Table S4 of the Supplementary material for details). This SoC-dependent behavior is generally consistent with charge-transfer processes occurring at the electrodes' interfaces [101,102]. The related DRT function in Fig. 6(b) deconvolutes the different semicircles into peaks according to their relaxation frequencies [56], while the small hump centered at $f = 10^{-2}$ Hz (labeled as *) is an artifact due to the removal of the Warburg diffusion. The small peak labeled as *P1* in the high-frequency range (i.e., 10^3 Hz < f < 10^4 Hz) shows only minor changes in intensity and frequency throughout the whole cycle, and is therefore consistent with the contribution of the contact resistance (R_{cont}). The peak labeled as *P2* at high-to-medium frequencies (10^2 Hz < f < 10^3 Hz) is found to have a slight dependence from the SoC, with a shift to higher frequencies upon de-lithiation and a decreasing intensity. Lastly, peak *P3* in the low-frequency region, is the one that shows the highest dependency on the SoC, as it first decreases in intensity while shifting to higher frequencies (from f = 1 Hz to f = 10 Hz) and then moves back to the initial frequency, with a slight increase in intensity. Considering the frequency ranges of *P2* (R_2 in the equivalent circuit) and *P3* (R_3 in the equivalent circuit), the two peaks can be associated to the polarizations related to the Li metal counter electrode and the charge-transfer resistance of LFMP cathode, respectively, as already reported in literature for LFP [102]. In order to unambiguously assign these SoC-dependent peaks to the actual interfacial processes, the DRT functions for symmetrical Li|Li and LFMP|LFMP cells at different temperatures are reported in Fig. S8(a) of the Supplementary material alongside with that of Li|LFMP half-cell obtained at 2.0 V (i.e., lithiated state). In addition, the SSR vs. λ plots (Fig. S8b) and the Arrhenius plots of the Areal Specific Resistances (ASR) (Fig. S8c) are used to find out the correlation between resistances and temperature [103]. In agreement with the previous assignment, the peak *P1* at high frequencies identified in both symmetrical cells is attributed to particle-particle and particle-current collector contact since the related resistance ($R_1 = R_{cont}$) does not display any linear dependence on the temperature. The peak *P2* at medium frequencies is also encountered for the two symmetrical cells, while the related resistance shows a temperature-dependent behavior only in the Li|Li one (R^2 > 0.99). This trend suggests that *P2* in the Li|LFMP half-cell includes contributions from the cathode SPI and the Li counter electrode, with the latter being predominant ($R_2 = R_{Li}$) [101]. Instead, the peak *P3* in the low-frequency region is only observed for the LFMP|LFMP symmetrical cell, and the associated resistance changes linearly with the temperature (R^2 > 0.99), thus confirming the assignment of the semicircle at the low frequency to the charge transfer resistance of the LFMP electrode ($R_3 = R_{ct}$) [102]. The fitted Nyquist plots upon the lithiation process after removal of the diffusion line (Fig. 6c) still display a relatively constant R_e and R_{cont}, while the medium- and low-frequency semicircles (R_{Li} and R_{ct}) show a symmetric behavior as compared to the previous de-lithiation process, with a decrease in

diameter upon lithium insertion up to 3.5 V and a progressive increase until reaching the lower cut-off (see fitted values in Table S5 of the Supplementary material for details). The related DRT functions (Fig. 6d) reveal polarizations deconvoluted according to their different relaxation frequencies [56]. The data indicate a *P1* (R_{cont}) at high frequencies with unaltered intensity and frequency, while *P2* (R_{Li}) and *P3* (R_{ct}) with inverse trend as compared to the de-lithiation process. The former peak slightly shifts to lower frequencies and increases in intensity, while the latter slightly decreases in intensity and shifts to higher frequencies from $f \sim 1$ Hz to $f \sim 10$ Hz, then strongly increases in intensity when moving back to the initial frequency [102]. The polarization associated with the charge-transfer of LFMP (i.e., R_{ct} in the equivalent circuit and the related *P3* in the DRT function) is reported as a function of the SoC during the voltammetry cycle in Fig. 6(e), while the trend of all the contributions to the total impedance within the cycle is reported in Fig. S9 (Supplementary material). Interestingly, during the anodic scan R_{ct} gradually decreases from ~140 Ω to ~60 Ω, suddenly drops to ~5 Ω at about 3.5 V as de-lithiation begins, holds this low resistance until ~4.2 V where the oxidation of Fe^{2+} and Mn^{2+} ends yielding to large part of the cell capacity, and finally raises to ~40 Ω gradually until 4.6 V. Moreover, the related *P3* peak from the DRT functions shifts to higher frequencies, thus suggesting the fastening of the charge-transfer kinetics promoted by lithium extraction from 3.5 to 4.2 V [90]. During the reverse cathodic scan the R_{ct} shows an initial fluctuation from ~35 Ω to ~55 Ω and back to ~35 Ω upon lithium insertion from 4.6 to 4.2 V, and a subsequent decrease to ~20 Ω at 3.9 V and to ~5 Ω at 3.5 V in correspondence to the reduction of Mn^{3+} and Fe^{3+}, while the related *P3* peak increases in frequency as the charge-transfer kinetics improve. Further reduction to 3.3 V leads to a rapid increase of R_{ct} from ~5 Ω to ~50 Ω, and a gradual raise to ~130 Ω until 1.8V where the scan ends. To further evaluate this behavior, the Li^+ diffusion coefficient in LFMP is achieved from the slope (σ) of the linear plots in Fig. 6(f) of Warburg impedance (Z_W) vs. the square root of frequency ($\omega^{-1/2}$), using impedance spectra taken from Fig. S7 at potentials associated with the redox couples Fe^{2+}/Fe^{3+} (3.52 and 3.44 V vs. Li^+/Li) and Mn^{2+}/Mn^{3+} (4.08 and 3.92 V vs. Li^+/Li). Therefore, the Li^+ diffusion coefficient, D_{EIS} ($cm^2\ s^{-1}$), is calculated using the Eq. (3) [104]:

$$D_{EIS} = \frac{1}{2}\left(\frac{RT}{z^2F^2AC\sigma}\right)^2 \quad (3)$$

where R is the gas constant (8.314 J K^{-1} mol^{-1}), T is the temperature (K), $z = 1$ is the number of exchanged electrons, F is the Faraday constant (96485 C mol^{-1}), C is the Li^+ concentration within the olivine lattice (mol cm^{-3}), A is the electrode geometric area (0.785 cm^2). The resulting D_{EIS} trend shown in Fig. 6(g) suggests a faster ion transport within the olivine lattice in correspondence with the redox process Fe^{+2}/Fe^{+3} (~5×10^{-12} $cm^2\ s^{-1}$) than the redox process Mn^{+2}/Mn^{+3} (6-8×10^{-13} $cm^2\ s^{-1}$), as already observed for D_{CV} in Fig. 4(c). In addition, the D_{EIS} are smaller than D_{CV} (Fig. 4c) and D_{GITT} (Fig. 5e), i.e., with values ~10^{-12} $cm^2\ s^{-1}$ as compared to 10^{-10} $cm^2\ s^{-1}$ at the same SoC. These differences could be ascribed to the use of different electrochemical techniques (i.e., different electrochemical equilibrium conditions depending on the applied signal), as mentioned in previous works [26]. The ion diffusion coefficients

reflect in fact the different electrochemical equilibrium conditions foreseen by the various electrochemical techniques. Hence, the ion transport is a consequence of the formation of a concentration gradient on the surface layer, which is achieved within a potentiostatic conditions according to Nernst equation in CV and EIS [89,92,95]. Therefore, D_{CV} and D_{EIS} could be representative for a theoretical and sensitive setup, which may however differ from the practical operation of the cell. Instead, GITT is a galvanostatic technique, and the related results could be more easily associated with the effective cyclic behavior of the material, as the insertion/de-insertion processes proceed in the battery. Hence, D_{GITT} may be considered the most representative method for cells under operating conditions [95,96]. Nevertheless, all the diffusion coefficients show comparable trends, especially when comparing D_{EIS} and D_{CV}, thus suggesting the accuracy and reliability of all the electrochemical methods adopted herein. Accordingly, the results point out a relevant reversibility of the processes within the mixed olivine, with a fast charge-transfer upon (de-)lithiation.

Journal Pre-proofs

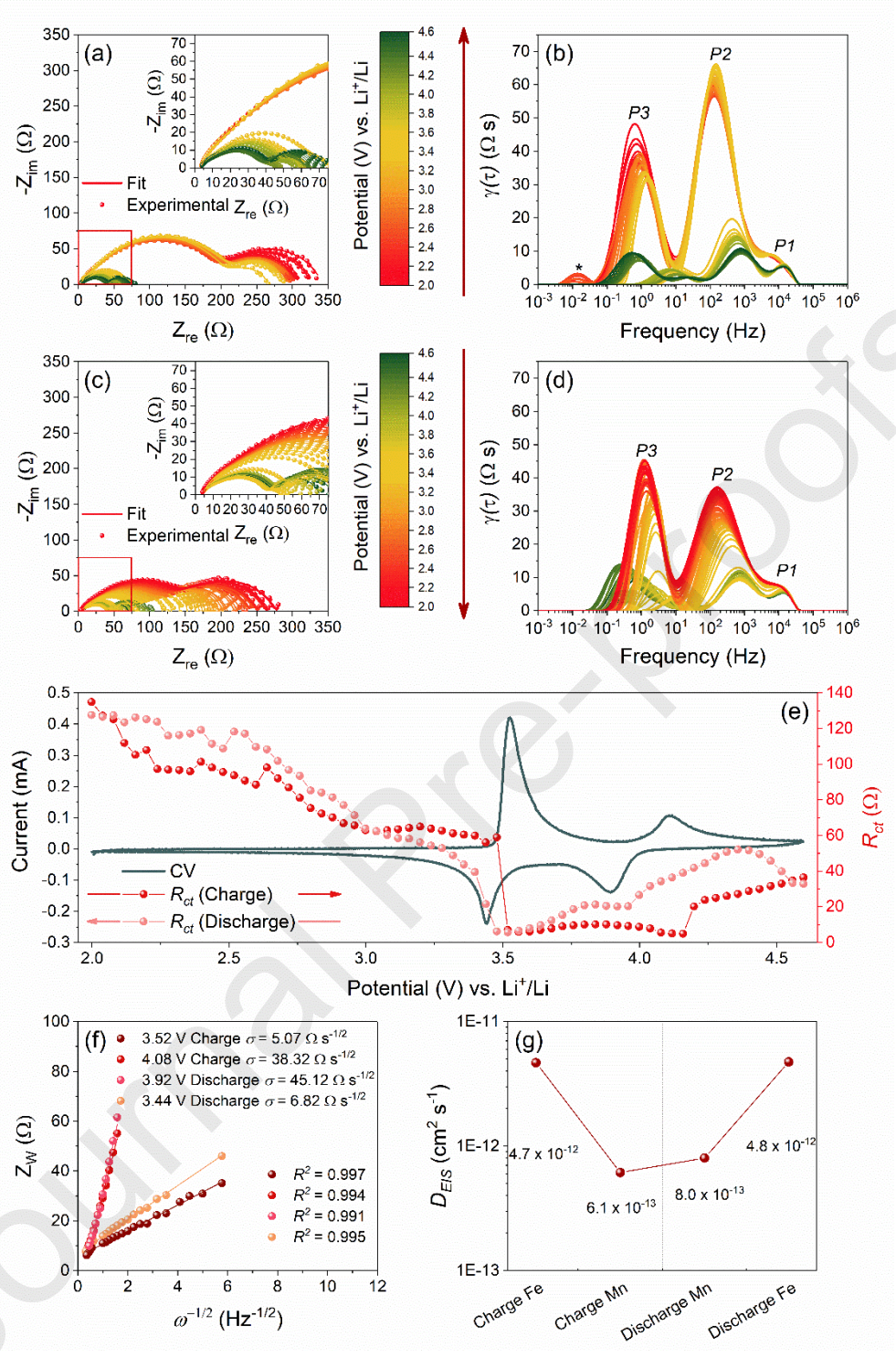

Fig. 6. SPEIS analysis of LFMP electrode in Li-cell. Nyquist plots after subtraction of the diffusive contribute, and related DRT analyses in terms of γ-factor vs. frequency with associated peak indexing obtained during (a and b) de-lithiation and (c and d) lithiation process, respectively. Inset in (a) and (c): magnification of the high-frequency region. (e) Trend of R_{ct} (right axis) and current (left axis) as a function of electrode potential during CV. (f) Plots of Z_W (Warburg impedance) vs. frequency$^{-1/2}$ with related linear fits and corresponding R^2 achieved upon determination of σ (Warburg coefficient). (g) Values of D_{EIS} (diffusion coefficient

from EIS) determined by using Eq. (3) for the Nyquist plots of Fig. S7 at 3.52, 4.08, 3.92, and 3.44 V vs. Li^+/Li. EIS collected during the 3rd cycle with sampling interval of about 40 mV, within the potential range 2.0 – 4.6 V vs. Li^+/Li, in the frequency range 200 kHz – 10 mHz and with an alternating voltage signal of 10 mV. DRT calculations performed according to Tikhonov regularization with an optimal λ-value of 10^{-2} and assuming a Gaussian distribution. Room temperature (25 °C). See the experimental section for acronyms.

The SPEIS protocol illustrated for LFMP is repeated hereafter to investigate the interfacial and Na^+ transport properties of NFMP, and the results are reported in Fig. 7. The Nyquist plots obtained upon the electrochemical process of NFMP in Na-cell in Fig. S10 (Supplementary material) display similar features as compared to LFMP (see Fig. S7), however with higher impedance values suggesting a more resistive interphase for the former cell compared with the latter one. After pre-processing, the fitted spectra upon de-sodiation (Fig. 7a) show relatively constant R_e and R_{cont}, progressive decrease of R_2 and R_3 until 3.0 V, and slight increase after 3.5 V (see fitted values in Table S6 of the Supplementary material). The sodiation process (Fig. 7c) leads to an analogue but less remarked change of R_2 and R_3, with a decrease upon sodium insertion up to 2.7 V and subsequent increase until reaching the lower cut-off, while R_e and R_{cont} remain almost unaltered (see fitted values in Table S7 of the Supplementary material). The DRT analysis with deconvolution of the various contributions to polarizations in three main peaks is reported in Fig. 7(b) during desodiation and in Fig. 7(d) during sodiation of NFMP in Na-cell, while the peak assignment is verified by the analysis of the symmetrical Na|Na and NFMP|NFMP cells in Fig. S11(a–c) (Supplementary material). During sodiation, Fig. 7(b) evidences that the peak *P1* related to R_{cont} is unchanged, with frequency values close to LFMP, instead the *P2* (polarizations of Na metal, R_2) and *P3* (charge-transfer resistance of NFMP, R_3) initially shift to higher frequencies and decrease in intensity, and then move back to the initial frequencies and slightly increase in intensity [101,102]. The DRT functions analysis related to the subsequent sodiation process (Fig. 7d) displays minor changes of *P1*, and an inverse trend of *P2* and *P3* as compared to the de-sodiation, with initial intensity decrease and shift to higher frequency indicating a faster charge-transfer, and following intensity increase while moving back to the initial frequency. Interestingly, the frequency shift of $P2/R_{Na}$ and $P3/R_{ct}$ in NFMP upon (de-)sodiation are much less pronounced and the corresponding frequencies reach lower values as compared to those of LFMP. This behavior indicates that the higher ionic radius of Na^+ hinders the charge-transfer kinetics and avoids the shift to the higher frequencies of the processes [87]. The above discussed data suggest once again a more challenging interphase with higher resistance and a limited ion diffusion in NFMP compared with LFMP, mainly due to kinetic issues associated with the higher volume of sodium than lithium, and with the resulting structural frictions within the olivine framework. Fig. 7(e) overlaps R_{ct} of NFMP with the cyclic voltammetry in Na-cell, while Fig. S12 (Supplementary material) shows the overall

contributions to the impedance. Remarkably, NFMP reveals an analogue trend to LFMP (compare Figs. 6e and 7e), however with a different feature due to the different alkali ion. Indeed, the Mn redox activity appears weakened in NFMP by the increased Jahn-Teller effect [45,46], and the resistance variation within the potential range of the redox activities is less pronounced. Hence, R_{ct} progressively decreases from ~150 Ω to ~100 Ω upon charging from 1.8 to 2.9 V, rapidly decreases to ~40 Ω at about 3.0 V, maintains almost the same value until ~3.5 V, and progressively increases to ~100 Ω at the charge cutoff (4.3 V). During the subsequent sodiation, the R_{ct} value initially increases to ~140 Ω by discharging until ~4V, then starts decreasing gradually until ~3.4 V to reach ~90 Ω and more rapidly until ~3.1 V to ~45 Ω, slightly fluctuates from 3 V to 2.7 V to a value of ~60 Ω, and then increases and holds a value of ~70 Ω from 2.6 V to the end of the discharge at 1.8 V. Despite less evident changes compared to LFMP, the trend of *Rct* described above is consistent with the activation of the redox processes Mn^{2+}/Mn^{3+} and Fe^{2+}/Fe^{3+} in correspondence to the related peaks in the voltammetry cycle. The Na^+ diffusion coefficient in NFMP is calculated according to the Warburg equation [104], using σ achieved from the plots of Z_w vs $\omega^{-1/2}$ (Fig. 7f) from specific impedance spectra of Fig. S10 of the redox processes Fe^{2+}/Fe^{3+} (Fe^A at 2.98 and 2.87 V vs. Na^+/Na, and Fe^B at 3.14 and 3.03 V vs. Na^+/Na) and Mn^{2+}/Mn^{3+} (at 3.86 and 3.52 V vs. Na^+/Na). The D_{EIS} trend in Fig. 7(g) remarks the higher transport properties within the olivine lattice in correspondence with Fe^{2+}/Fe^{3+} redox couple then Mn^{2+}/Mn^{3+} one, which is a trend in line with the data achieved by CV and GITT, however with lower values at comparable SoC, i.e., of about 10^{-14} cm^2 s^{-1} for D_{EIS} as compared to 10^{-12} cm^2 s^{-1} for D_{GITT} and D_{CV} (see Fig. 4d and Fig. 5e, respectively).

Journal Pre-proofs

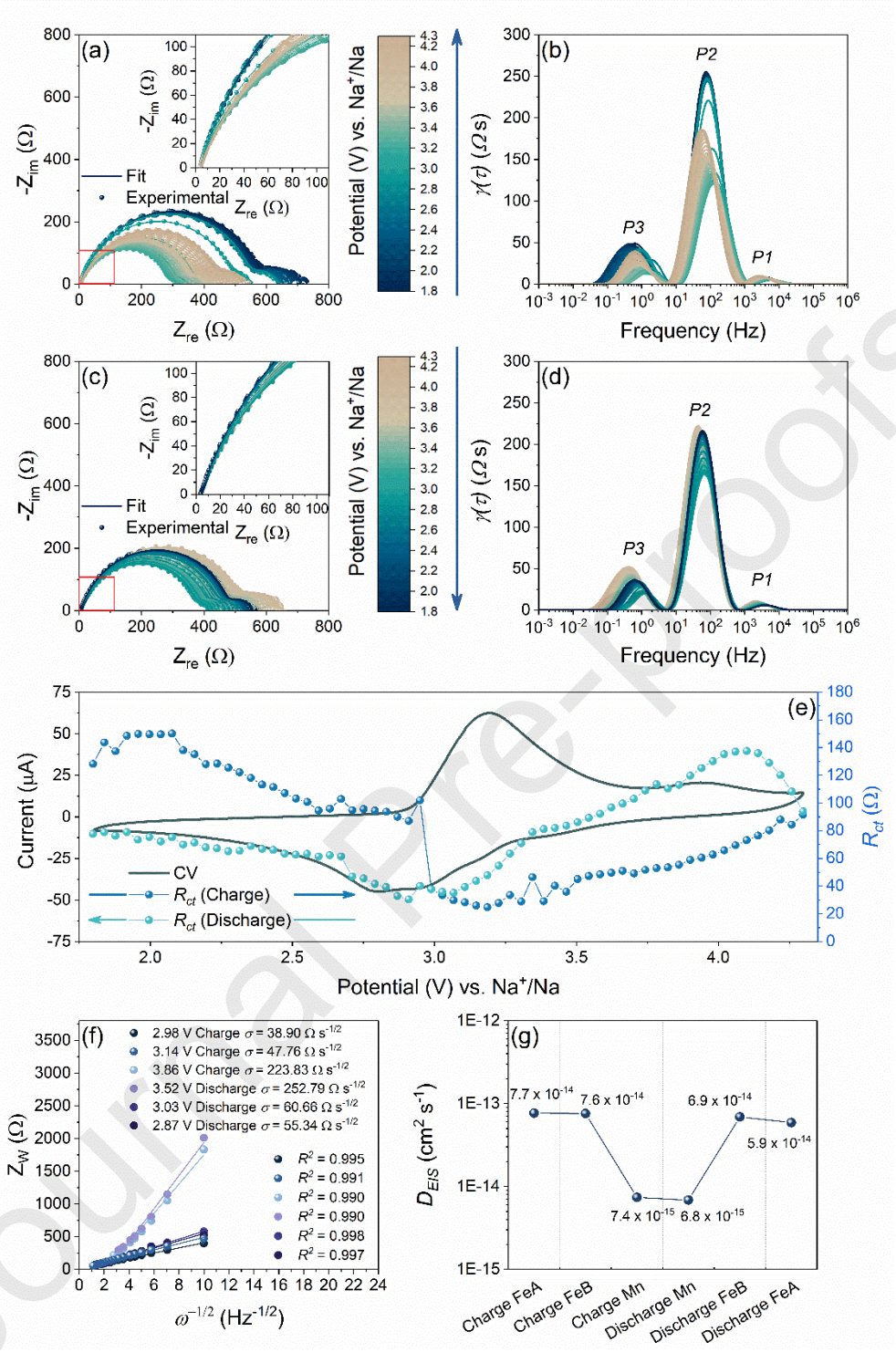

Fig. 7. SPEIS analysis of NFMP electrode in Na-cell. Nyquist plots after subtraction of the diffusive contribute, and related DRT analyses in terms of γ-factor vs. frequency with associated peak indexing obtained during (a and b) de-lithiation and (c and d) lithiation process, respectively. Inset in (a) and (c): magnification of the high-frequency region. (e) Trend of R_{ct} (right axis) and current (left axis) as a function of electrode potential during CV. (f) Plots of Z_W (Warburg impedance) vs. frequency$^{-1/2}$ with related linear fits and corresponding R^2 achieved upon determination of σ (Warburg coefficient). (g) Values of D_{EIS} (diffusion coefficient

from EIS) determined by using Eq. (3) for the Nyquist plots of Fig. S10 at 2.98, 3.14, 3.86, 3.52, 3.03, and 2.87 V vs. Na^+/Na. EIS collected during the 3rd cycle with sampling interval of about 40 mV, within the potential range 1.8 – 4.3 V vs. Na^+/Na, in the frequency range 200 kHz – 10 mHz and with an alternating voltage signal of 10 mV. DRT calculations performed according to Tikhonov regularization with an optimal λ-value of 10^{-2} and assuming a Gaussian distribution. Room temperature (25 °C). See the experimental section for acronyms.

The results obtained from the interfacial analysis in terms of R_{ct} for the LFMP and NFMP mixed olivines display a very similar behavior upon Li or Na (de-)insertion, despite the different reaction kinetics related to the characteristic ion mobility which favors in general lithium with respect to sodium [26,45,87]. Hence, the relevant Jahn-Teller distortion promoted by the Mn can hinder the transport of the voluminous sodium ion. On the other hand, the decrease of the diffusion coefficient in Mn sites is principally ascribed to the lower ionic conductivity of the de-lithiated/de-sodiated phase of the olivine compared to the pristine one, particularly over the extraction of more than a half of the overall Li^+/Na^+ occurring upon Fe^{2+}/Fe^{3+} redox process [90].

4. Conclusions

A NFMP sodium-mixed olivine cathode is achieved in this work by the electrochemical de-lithiation of the analogue lithium-based electrode and subsequent sodiation process. The study indicates that LFMP is successfully converted to NFMP with a well-defined structure without any impurity, as confirmed by XRD and Raman spectroscopy. SEM/EDS revealed for NFMP suitable morphology with homogeneous distribution of the elements in the electrode, allowing a reversible electrochemical process of Fe^{2+}/Fe^{3+} and Mn^{2+}/Mn^{3+} redox couples in sodium cell at 3.0, 3.2, and 3.8 V vs. Na^+/Na, respectively. The data also suggested for the mixed olivine based on iron and manganese a different electrochemical reaction mechanism as compared with the pure iron olivine. In fact, CV measurement revealed two redox processes for Fe^{2+}/Fe^{3+} (Fe^A at 2.98 and 2.87 V vs. Na^+/Na, and Fe^B 3.14 and 3.03 V vs. Na^+/Na) and a single one for Mn^{2+}/Mn^{3+} (at 3.86 and 3.52 V vs. Na^+/Na) in NFMP, instead of the one centered at about 3.0 V vs. Na^+/Na associated with the Fe^{3+}/Fe^{2+} in NFP observed in literature. Tests in sodium cells of NFMP have shown a maximum capacity exceeding 100 mAh g^{-1} at 55 °C and a satisfactory rate capability from C/20 to 2C rate at room temperature. The achieved capacity values and the average working voltage of the cells suggested possible improvement of the energy density of the material by optimizing the Fe/Mn ratio. Moreover, the comparison of ion transport and interfacial properties of LFMP with NFMP indicated for the latter slower kinetics and more resistive interphase of the cell, as expected by the higher Na^+ dimensions and more relevant reactivity of the alkali metal. Relevantly, the data have shown for NFMP ion transport and charge-transfer behavior analogue to that of LFMP, thus suggesting the actual possibility of exploiting the mixed olivine as an efficient

cathode in sodium cell. The ion diffusion coefficients in NFMP and LFMP have been achieved by CV, GITT and SPEIS. The related trends confirmed faster transport within the olivine lattice of NFMP in correspondence with Fe^{2+}/Fe^{3+} redox couple then Mn^{2+}/Mn^{3+} one, in line with the data achieved by CV and GITT, however with lower values for D_{EIS} (~10^{-14} cm^2 s^{-1}) as compared to D_{GITT} and D_{CV} (~10^{-12} cm^2 s^{-1}). The results of this work can rationalize the behavior of the mixed olivine in terms of the reaction mechanism and ion transport, and shed light on the possibility of achieving a low-cost and environmental friendly cathode with similar structural stability, ion transport, and interfacial properties compared to lithium olivine. Despite the result of this work suggested the increase of the temperature to 55 °C as possible pathway to achieve a higher capacity, we believe that NFMP cathode may be definitely improved by further tuning the material composition in terms of Fe to Mn ratio to limit the Jahn-Teller distortion in olivines with high Mn content.

Acknowledgments

The work was performed within the grant "Fondo di Ateneo per la Ricerca Locale (FAR) 2022", University of Ferrara, and the collaboration project "Accordo di Collaborazione Quadro 2015" between University of Ferrara (Department of Chemical and Pharmaceutical Sciences) and Sapienza University of Rome (Department of Chemistry). J.H. and V.M. thank the European Union's Horizon 2020 research and innovation programme Graphene Flagship, grant agreement No 881603.

References

[1] P.T. Moseley, J. Garche, Electrochemical Energy Storage for Renewable Sources and Grid Balancing, Elsevier, 2015.

[2] O. Ellabban, H. Abu-Rub, F. Blaabjerg, Renew. Sustain. Energy Rev. 39 (2014) 748–764.

[3] D. Larcher, J.M. Tarascon, Nat. Chem. 7 (2015) 19–29.

[4] B. Scrosati, K.M. Abraham, W.A. van. Schalkwijk, Jusef. Hassoun, Lithium Batteries : Advanced Technologies and Applications. Wiley, 2013.

[5] M. Armand, J.-M. Tarascon, Nature 451 (2008) 652–657.

[6] J. Neubauer, E. Wood, J. Power Sources 259 (2014) 262–275.

[7] P.S. Grant, D. Greenwood, K. Pardikar, R. Smith, T. Entwistle, L.A. Middlemiss, G. Murray, S.A. Cussen, M.J. Lain, M.J. Capener, M. Copley, C.D. Reynolds, S.D. Hare, M.J.H. Simmons, E. Kendrick, S.P. Zankowski, S. Wheeler, P. Zhu, P.R. Slater, Y.S. Zhang, A.R.T. Morrison, W. Dawson, J. Li, P.R. Shearing, D.J.L. Brett, G. Matthews, R. Ge, R. Drummond, E.C. Tredenick, C. Cheng, S.R. Duncan, A.M. Boyce, M. Faraji-Niri, J. Marco, L.A. Roman-Ramirez, C. Harper, P. Blackmore, T. Shelley, A. Mohsseni, D.J. Cumming, J. Phys. Energy 4 (2022) 042006.

Journal Pre-proofs

[8] B. Scrosati, J. Hassoun, Y.K. Sun, Energy Environ. Sci. 4 (2011) 3287–3295.

[9] M. Ntombela, K. Musasa, K. Moloi, World Elec. Veh. J. 14 (2023) 195.

[10] D. Di Lecce, R. Verrelli, J. Hassoun, Green Chem. 19 (2017) 3442–3467.

[11] T.P. Narins, Extr. Ind. Soc. 4 (2017) 321–328.

[12] N. Yabuuchi, K. Kubota, M. Dahbi, S. Komaba, Chem. Rev. 114 (2014) 11636–11682.

[13] M.M. Thackeray, C. Wolverton, E.D. Isaacs, Energy Environ. Sci. 5 (2012) 7854–7863.

[14] M. Baumann, M. Häringer, M. Schmidt, L. Schneider, J.F. Peters, W. Bauer, J.R. Binder, M. Weil, Adv. Energy Mater. 12 (2022) 2202636.

[15] I. Hasa, J. Hassoun, S. Passerini, Nano Res. 10 (2017) 3942–3969.

[16] P.K. Nayak, L. Yang, W. Brehm, P. Adelhelm, Angew. Chem. Int. Ed. 57 (2018) 102–120.

[17] A.K. Padhi, K.S. Nanjundaswamy, J.B. Goodenough, J. Electrochem. Soc. 144 (1997) 1188–1194.

[18] L.-X. Yuan, Z.-H. Wang, W.-X. Zhang, X.-L. Hu, J.-T. Chen, Y.-H. Huang, J.B. Goodenough, Energy Environ. Sci. 4 (2011) 269–284.

[19] J.B. Goodenough, K.-S. Park, J. Am. Chem. Soc. 135 (2013) 1167–1176.

[20] Y. Wang, P. He, H. Zhou, Energy Environ. Sci. 4 (2011) 805–817.

[21] L. Minnetti, V. Marangon, P. Andreotti, A. Staffolani, F. Nobili, J. Hassoun, Electrochim. Acta 452 (2023) 142263.

[22] D. Di Lecce, R. Brescia, A. Scarpellini, M. Prato, J. Hassoun, ChemSusChem 9 (2016) 223–230.

[23] D. Di Lecce, V. Gancitano, J. Hassoun, ACS Sustain. Chem. Eng. 8 (2020) 278–289.

[24] L. Minnetti, V. Marangon, J. Hassoun, Adv. Sustain. Syst. 6 (2022) 2100464.

[25] B. Zhang, X. Wang, H. Li, X. Huang, J. Power Sources 196 (2011) 6992–6996.

[26] D. Di Lecce, J. Hassoun, J. Phys. Chem. C 119 (2015) 20855–20863.

[27] Z.X. Nie, C.Y. Ouyang, J.Z. Chen, Z.Y. Zhong, Y.L. Du, D.S. Liu, S.Q. Shi, M.S. Lei, Solid State Commun. 150 (2010) 40–44.

Journal Pre-proofs

[28] A. Yamada, S.-C. Chung, J. Electrochem. Soc. 148 (2001) A960.

[29] L. Yang, W. Deng, W. Xu, Y. Tian, A. Wang, B. Wang, G. Zou, H. Hou, W. Deng, X. Ji, J. Mater. Chem. A 9 (2021) 14214–14232.

[30] A. Yamada, Y. Kudo, K.-Y. Liu, J. Electrochem. Soc. 148 (2001) A747.

[31] D. Di Lecce, T. Hu, J. Hassoun, J. Alloys Compd. 693 (2017) 730–737.

[32] L. He, H. Li, X. Ge, S. Li, X. Wang, S. Wang, L. Zhang, Z. Zhang, Adv. Mater. Interfaces 9 (2022) 2200515.

[33] I. Hasa, J. Hassoun, Y.K. Sun, B. Scrosati, ChemPhysChem 15 (2014) 2152–2155.

[34] I. Hasa, S. Mariyappan, D. Saurel, P. Adelhelm, A.Y. Koposov, C. Masquelier, L. Croguennec, M. Casas-Cabanas, J. Power Sources 482 (2021) 228872.

[35] I.U. Mohsin, L. Schneider, Z. Yu, W. Cai, C. Ziebert, Int. J. Electrochem. 2023 (2023) 1–9.

[36] M. Avdeev, Z. Mohamed, C.D. Ling, J. Lu, M. Tamaru, A. Yamada, P. Barpanda, Inorg. Chem. 52 (2013) 8685–8693.

[37] J. Hwang, K. Matsumoto, T. Nohira, R. Hagiwara, Electrochem. 85 (2017) 675–679.

[38] J. Hwang, K. Matsumoto, Y. Orikasa, M. Katayama, Y. Inada, T. Nohira, R. Hagiwara, J. Power Sources 377 (2018) 80–86.

[39] S. Jana, G. Lingannan, M. Ishtiyak, G. Panigrahi, A. Sonachalam, J. Prakash, Mater. Res. Bull. 126 (2020) 110835.

[40] C. Berlanga, I. Monterrubio, M. Armand, T. Rojo, M. Galceran, M. Casas-Cabanas, ACS Sustain. Chem. Eng. 8 (2020) 725–730.

[41] S.M. Oh, S.T. Myung, J. Hassoun, B. Scrosati, Y.K. Sun, Electrochem. Commun. 22 (2012) 149–152.

[42] B. Swain, Sep. Purif. Technol. 172 (2017) 388–403.

[43] S. Altundag, S. Altin, S. Yaşar, E. Altin, Vacuum 210 (2023) 111853.

[44] E. Gucciardi, M. Galceran, A. Bustinza, E. Bekaert, M. Casas-Cabanas, J. Phys: Mater. 4 (2021) 034002.

[45] D. Saurel, M. Giner, M. Galceran, J. Rodríguez-Carvajal, M. Reynaud, M. Casas-Cabanas, Electrochim. Acta 425 (2022) 140650.

Journal Pre-proofs

[46] C. Henriksen, J.K. Mathiesen, Y.M. Chiang, K.M.Ø. Jensen, D.B. Ravnsbæk, ACS Appl. Energy Mater. 2 (2019) 8060–8067.

[47] K.T. Lee, T.N. Ramesh, F. Nan, G. Botton, L.F. Nazar, Chem. Mater. 23 (2011) 3593–3600.

[48] L. Lutterotti, Nucl. Instrum. Methods Phys. Res. B 268 (2010) 334–340.

[49] X.Y. Li, B. Zhang, Z.G. Zhang, L.H. He, H. Li, X.J. Huang, F.W. Wang, Powder Diffr. 29 (2014) 248–253.

[50] M. Kopeć, A. Yamada, G. Kobayashi, S. Nishimura, R. Kanno, A. Mauger, F. Gendron, C.M. Julien, J. Power Sources 189 (2009) 1154–1163.

[51] P.B. Moore, Am. Min. 57 (1972) 1333–1344.

[52] M. Li, C. Wang, Z. Chen, K. Xu, J. Lu, Chem. Rev. 120 (2020) 6783–6819.

[53] B. Boukamp, Solid State Ion. 20 (1986) 31–44.

[54] B. Boukamp, Solid State Ion. 18–19 (1986) 136–140.

[55] F. Ciucci, C. Chen, Electrochim. Acta 167 (2015) 439–454.

[56] A.L. Gavrilyuk, D.A. Osinkin, D.I. Bronin, Russ. J. Electrochem. 53 (2017) 575–588.

[57] S.W. Oh, S.T. Myung, S.M. Oh, K.H. Oh, K. Amine, B. Scrosati, Y.K. Sun, Adv. Mater. 22 (2010) 4842–4845.

[58] D. Saurel, M. Galceran, M. Reynaud, H. Anne, M. Casas-Cabanas, Int. J. Energy Res. 42 (2018) 3258–3265.

[59] T. Muraliganth, A. Manthiram, J. Phys. Chem. C 114 (2010) 15530–15540.

[60] A.S. Cooper, Acta Crystallogr. 15 (1962) 578–582.

[61] B.H. Toby, Powder Diffr. 21 (2006) 67–70.

[62] L.B. Mccusker, R.B. Von Dreele, D.E. Cox, D. Loue, P. Scardi, J. Appl. Cryst. 32 (1999) 36–50.

[63] R. Gupta, S. Saha, M. Tomar, V.K. Sachdev, V. Gupta, J. Mater. Sci. Mater. Electron. 28 (2017) 5192–5199.

[64] W. Wazeer, M.M. Nabil, M. Feteha, M.B. Soliman, A.E.-H.B. Kashyout, Sci. Rep. 12 (2022) 16307.

[65] T. Boyadzhieva, V. Koleva, E. Zhecheva, D. Nihtianova, L. Mihaylov, R.

Journal Pre-proofs

Stoyanova, RSC Adv. 5 (2015) 87694–87705.

[66] B. Özdogru, H. Dykes, S. Padwal, S. Harimkar, Ö.Ö. Çapraz, Electrochim. Acta 353 (2020) 136594.

[67] R. Malik, F. Zhou, G. Ceder, Phys. Rev. B 79 (2009) 214201.

[68] K. Zaghib, J. Trottier, P. Hovington, F. Brochu, A. Guerfi, A. Mauger, C.M. Julien, J. Power Sources 196 (2011) 9612–9617.

[69] G. Kobayashi, A. Yamada, S. Nishimura, R. Kanno, Y. Kobayashi, S. Seki, Y. Ohno, H. Miyashiro, J. Power Sources 189 (2009) 397–401.

[70] A. Saracibar, J. Carrasco, D. Saurel, M. Galceran, B. Acebedo, H. Anne, M. Lepoitevin, T. Rojo, M. Casas Cabanas, Phys. Chem. Chem. Phys. 18 (2016) 13045–13051.

[71] M. Galceran, V. Roddatis, F.J. Zúñiga, J.M. Pérez-Mato, B. Acebedo, R. Arenal, I. Peral, T. Rojo, M. Casas-Cabanas, Chem. Mater. 26 (2014) 3289–3294.

[72] M.Á. Muñoz-Márquez, D. Saurel, J.L. Gómez-Cámer, M. Casas-Cabanas, E. Castillo-Martínez, T. Rojo, Adv. Energy Mater. 7 (2017) 1700463.

[73] J. Wang, Z. Xu, Q. Zhang, X. Song, X. Lu, Z. Zhang, A.J. Onyianta, M. Wang, M. Titirici, S.J. Eichhorn, Adv. Mater. 34 (2022) 2206637.

[74] U. Purushotham, N. Takenaka, M. Nagaoka, RSC Adv. 6 (2016) 65232–65242.

[75] D. Di Lecce, L. Minnetti, D. Polidoro, V. Marangon, J. Hassoun, Ionics 25 (2019) 3129–3141.

[76] V. Marangon, L. Minnetti, M. Adami, A. Barlini, J. Hassoun, Energy and Fuels 35 (2021) 10284–10292.

[77] L. Carbone, S. Munoz, M. Gobet, M. Devany, S. Greenbaum, J. Hassoun, Electrochim. Acta 231 (2017) 223–229.

[78] A. Yamada, M. Hosoya, S.C. Chung, Y. Kudo, K. Hinokuma, K.Y. Liu, Y. Nishi, J. Power Sources 119–121 (2003) 232–238.

[79] M. Giner, V. Roddatis, C.M. López, P. Kubiak, J. Electrochem. Soc. 163 (2016) A650–A653.

[80] F. Bianchini, H. Fjellvåg, P. Vajeeston, Mater. Chem. Phys. 219 (2018) 212–221.

[81] N. Phattharasupakun, P. Bunyanidhi, P. Chiochan, N. Chanlek, M. Sawangphruk, Electrochem. Commun. 139 (2022) 107309.

Journal Pre-proofs

[82] V. Marangon, C. Hernández-Rentero, M. Olivares-Marín, V. Gómez-Serrano, Á. Caballero, J. Morales, J. Hassoun, ChemSusChem 14 (2021) 3333–3343.

[83] D.H. Baek, J.K. Kim, Y.J. Shin, G.S. Chauhan, J.H. Ahn, K.W. Kim, J. Power Sources 189 (2009) 59–65.

[84] Y. Wang, Z. Cao, Z. Ma, G. Liu, H. Cheng, Y. Zou, L. Cavallo, Q. Li, J. Ming, ACS Energy Lett. 8 (2023) 1477–1484.

[85] Y. Pan, L. Gong, Y. Fu, L. Shi, C. Liu, Y. Pan, J. Yang, H. Zhang, X. Cheng, Energy Storage Mater. 52 (2022) 238–249.

[86] Y. Wang, Z. Cao, W. Wahyudi, Z. Ma, Y. Liang, L. Cavallo, Q. Li, J. Ming, Adv. Energy Mater. 13 (2023) 2301354.

[87] Y. Zhu, Y. Xu, Y. Liu, C. Luo, C. Wang, Nanoscale 5 (2013) 780–787.

[88] A. Ponrouch, D. Monti, A. Boschin, B. Steen, P. Johansson, M.R. Palacín, J. Mater. Chem. A 3 (2015) 22–42.

[89] J.E.B. Randles, Discuss. Faraday Soc. 1 (1947) 11–19.

[90] M. Yonemura, A. Yamada, Y. Takei, N. Sonoyama, R. Kanno, J. Electrochem. Soc. 151 (2004) A1352–A1356.

[91] S. Brutti, J. Hassoun, B. Scrosati, C.-Y. Lin, H. Wu, H.-W. Hsieh, J. Power Sources 217 (2012) 72–76.

[92] W. Weppner, R.A. Huggins, J. Electrochem. Soc. 124 (1977) 1569–1578.

[93] K. Tang, X. Yu, J. Sun, H. Li, X. Huang, Electrochim. Acta 56 (2011) 4869–4875.

[94] C. Heubner, S. Heiden, M. Schneider, A. Michaelis, Electrochim. Acta 233 (2017) 78–84.

[95] S.D. Kang, W.C. Chueh, J. Electrochem. Soc. 168 (2021) 120504.

[96] Z. Geng, Y.-C. Chien, M.J. Lacey, T. Thiringer, D. Brandell, Electrochim. Acta 404 (2022) 139727.

[97] L. Sbrascini, A. Staffolani, L. Bottoni, H. Darjazi, L. Minnetti, M. Minicucci, F. Nobili, ACS Appl. Mater. Interfaces 14 (2022) 33257–33273.

[98] A. Baldinelli, A. Staffolani, F. Nobili, L. Barelli, J. Energy Storage 73 (2023) 109117.

[99] A. Staffolani, A. Baldinelli, G. Bidini, F. Nobili, L. Barelli, Energies 15 (2022) 4978.

Journal Pre-proofs

[100] A.Ch. Lazanas, M.I. Prodromidis, ACS Meas. Sci. Au 3 (2023) 162–193.

[101] B. Manikandan, V. Ramar, C. Yap, P. Balaya, J. Power Sources 361 (2017) 300–309.

[102] J. Illig, M. Ender, T. Chrobak, J.P. Schmidt, D. Klotz, E. Ivers-Tiffée, J. Electrochem. Soc. 159 (2012) A952–A960.

[103] J.P. Schmidt, T. Chrobak, M. Ender, J. Illig, D. Klotz, E. Ivers-Tiffée, J. Power Sources 196 (2011) 5342–5348.

[104] G. Barbero, I. Lelidis, Phys. Chem. Chem. Phys. 19 (2017) 24934–24944.

Graphical Abstract

A $NaFe_{0.6}Mn_{0.4}PO_4$ (NFMP) cathode is obtained from lithium analogue (LFMP) through electrochemical conversion (left-side image), and investigated in terms of ion diffusion (middle-side image) and interphase properties (right-side image).

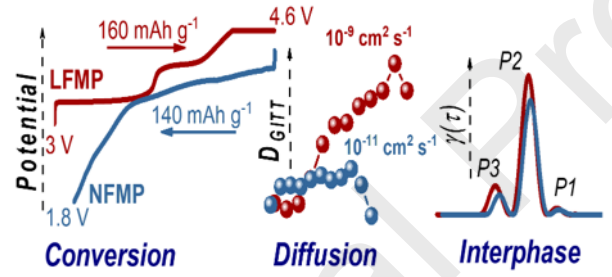

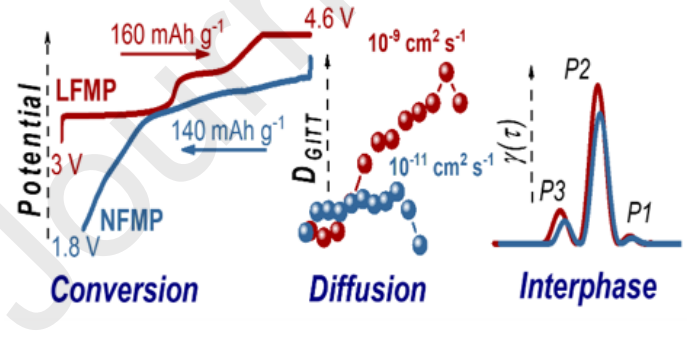

Declaration of interests

☐ The authors declare that they have no known competing financial interests or personal

relationships that could have appeared to influence the work reported in this paper.

☒ The authors declare the following financial interests/personal relationships which may be considered as potential competing interests:

Jusef Hassoun reports a relationship with University of Ferrara that includes: employment and funding grants. Jusef Hassoun reports a relationship with Italian Institute of Technology that includes: funding grants. If there are other authors, they declare that they have no known competing financial interests or personal relationships that could have appeared to influence the work reported in this paper.

Journal Pre-proofs